

Quantum simulation of the Dicke model in a two-dimensional ion crystal: chaos, quantum thermalization, and revivals

Bryce Bullock,^{1,*} Sean R. Muleady,^{2,3,†} Jennifer F. Lilieholm,¹ Yicheng Zhang,⁴ Arghavan Safavi-Naini,^{5,6} Robert J. Lewis-Swan,⁴ John J. Bollinger,¹ Ana Maria Rey,^{7,8,‡} and Allison L. Carter¹

¹*National Institute of Standards and Technology, Boulder, Colorado 80309, USA*

²*Joint Center for Quantum Information and Computer Science, National Institute of Standards and Technology and University of Maryland, College Park, Maryland 20742, USA*

³*Joint Quantum Institute, National Institute of Standards and Technology and University of Maryland, College Park, Maryland 20742, USA*

⁴*Homer L. Dodge Department of Physics and Astronomy, The University of Oklahoma, Norman, Oklahoma 73019, USA and Center for Quantum Research and Technology, The University of Oklahoma, Norman, Oklahoma 73019, USA*

⁵*Institute of Physics, University of Amsterdam, Science Park 904, 1098 XH Amsterdam, the Netherlands*

⁶*QuSoft, Science Park 123, 1098 XG Amsterdam, the Netherlands*

⁷*JILA, National Institute of Standards and Technology and University of Colorado, 440 UCB, Boulder, Colorado 80309, USA*

⁸*Center for Theory of Quantum Matter, University of Colorado, Boulder, CO, 80309, USA*

(Dated: February 19, 2026)

Quantum many-body systems driven far from equilibrium can exhibit chaos, entanglement, and non-classical correlations, yet directly observing these phenomena in large, closed quantum systems remains challenging. Here we realize the Dicke model—a fundamental description of light-matter interactions—in a two-dimensional crystal of approximately 100 trapped ions. The ions’ internal state is optically coupled to the center of mass vibrational mode via an optical spin-dependent force, enabling unitary many-body dynamics beyond the mean-field and few-body limits. In the integrable regime, where the phonons can be adiabatically eliminated, we observe a dynamical phase transition between ferromagnetic to paramagnetic spin phases. In contrast, when the spins and phonons are strongly coupled, we observe clear signatures of non-integrable chaotic dynamics, including erratic phase-space trajectories and the exponential growth of excitations and entanglement quantified by the one-body Rényi entropy. By quenching from an unstable fixed point in the near-integrable regime, quantum noise can generate correlated spin-phonon excitations. Our numerical calculations, in clear agreement with experiment, reveal the generation of two-mode spin-phonon squeezing, 2.6 dB below the standard quantum limit (4.6 dB relative to the initial thermal state), followed by generalized vacuum Rabi collapses and revivals. Our results establish large ion crystals as scalable analog quantum simulators of non-equilibrium light-matter dynamics and provide a controlled platform for experimental studies of information scrambling and entanglement in closed many-body systems.

I. INTRODUCTION

Quantum simulators offer a direct way to explore interacting many-body systems far from equilibrium, where coherent dynamics can give rise to remarkably rich phenomena, including dynamical phase transitions, entanglement growth, and thermalization in the absence of an external bath. Beyond demonstrating these effects, an important open question is how familiar yet complex phenomena from classical nonlinear physics—such as dynamical instabilities and chaos—persist or otherwise break down once quantum correlations proliferate and entanglement becomes essential. Addressing this question in experimentally relevant systems remains challenging, as the exponential growth of the Hilbert space makes preserving coherent, unitary dynamics in larger quantum systems increasingly difficult.

Spin-boson models, which arise across fields ranging from condensed matter and quantum optics to molecular and chemical dynamics, provide a natural setting for experimentally investigating such complex questions. These models couple discrete, intrinsically quantum spin degrees of freedom with bosonic modes that can host a large occupation, mediating relaxation, transport, and collective behavior. Key among them, the Dicke model [1, 2], describing a collective spin coupled to a single bosonic mode, offers a minimal setting that supports a crossover between integrable and chaotic behavior [3–8]. Despite the Dicke model’s conceptual simplicity and broad theoretical significance, experimental access to its genuine quantum behaviors in scalable systems has remained out of reach [8–21]. Crucially, hallmark signatures of fully coherent Dicke dynamics—such as pair production, hybrid spin-boson squeezing, and collapse-and-revival phenomena arising from strong spin-boson entanglement—have not yet been observed.

Here, we realize the Dicke model in a closed, two-dimensional crystal of about 100 Be^+ ions confined in a Penning trap, where the collective spin is encoded in electronic spin states, and the center-of-mass motion plays

* These authors contributed equally.

† These authors contributed equally.; sean.muleady@gmail.com

‡ arey@jila1.colorado.edu

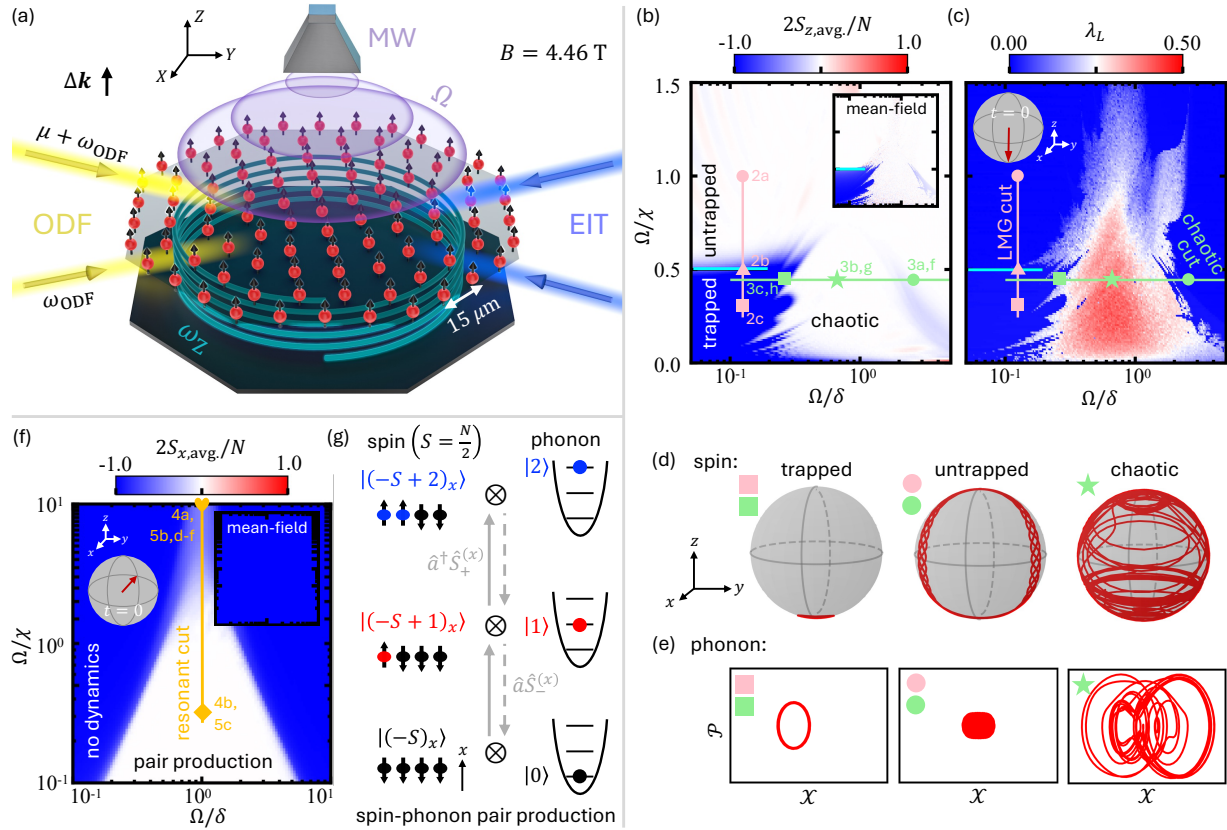


FIG. 1. Experimental setup and dynamical regimes. (a) $N \sim 10^2$ beryllium ions (red dots) are confined in a Penning trap, with an axial magnetic field $B = 4.46$ T. The Doppler-cooled ions form a 2D crystal, whose axial center-of-mass (COM) motion realizes a high-Q mechanical oscillator with frequency ω_Z (teal spring), and which may be further cooled by crossed electromagnetically induced transparency (EIT) beams (blue). Phonon excitations of this COM motion collectively couple to the ions' valence electronic spin at rate g , induced by a spin-dependent optical dipole force (ODF) from crossed optical beams (yellow) with relative wavevector $\Delta\mathbf{k}$ and frequency difference $\mu \equiv \delta + \omega_Z$. The spins can also be globally addressed by microwaves (MW, purple) with Rabi rate Ω . (b) Expected time-averaged magnetization and (c) classical Lyapunov exponent, λ_L , for spins initially polarized along $-z$, as a function of Ω/δ and Ω/χ , where $\chi \equiv 4g^2/\delta$; inset to (b) shows corresponding MF results. We consider two different experimental parameter sweeps: an “LMG cut” (pink line)—dominated by an effective, integrable LMG spin-spin interaction—which traverses a dynamical phase transition (cyan line) between spin-trapped and spin-untrapped behaviors; and a “chaotic cut” (green line), where the phonons play a more active role and can enable non-integrable chaotic behavior. Colored symbols label parameters considered later in the text, and we also show examples of corresponding classical dynamical trajectories of (d) the spins on the collective Bloch sphere and (e) the COM motion in canonical phase space $(\mathcal{X}, \mathcal{P})$. (f) Analogous time-averaged transverse magnetization and experimental sweep (“resonant cut”, orange line and symbols) for spins initially polarized along $-x$, which exhibits non-trivial dynamics close to resonance ($\Omega \sim \delta$), driven by quantum fluctuations for an initial bosonic vacuum state. Corresponding MF results in inset exhibit no dynamics. For $\Omega \gg \chi$, the build-up of entanglement manifests in the form of pair production of correlated spin-phonon excitations illustrated in (g). The spin excitations correspond to fully symmetrized spin flips along x , which occur together with a phonon excitation. This paired generation leads to exponential growth of mode populations from vacuum or thermal fluctuations and produces nonclassical correlations, including reduced fluctuations in collective quadratures characteristic of two-mode squeezing.

the role of the bosonic mode. Due to the highly coherent nature of this motion—with minimal dissipation and low heating rates on experimentally relevant timescales—this architecture enables us to gain full control of the spin-phonon degrees of freedom and observe a rich class of dynamical behaviors.

Consistent with prior investigations carried out in regimes where the bosonic mode can be adiabatically eliminated, we observe a dynamical phase transition between ferromagnetic and paramagnetic behavior [22–30].

Going beyond this integrable limit, we are able to push the dynamics into the non-integrable regime predicted to be chaotic at the mean-field (MF) level. There we find erratic phase-space trajectories and damping from quantum fluctuations, as expected from quantum scrambling.

We are also able to explore the fully quantum regime where classical dynamics predict no evolution by preparing the system near an unstable fixed point. In this case we observe exponential growth of excitations, consistent with correlated pair creation and entanglement buildup

driven by quantum vacuum noise. This results in quantum thermalization of local observables consistent with full numerical simulations of the one-body Rényi entropy inferred from experimental measurements. In the near-integrable regime where quantum noise drives correlated spin-phonon fluctuations, numerical simulations of the model accounting for experimental imperfections show a reduction in noise variance via two-mode squeezing reaching up to 2.6 dB below the standard quantum limit (4.6 dB relative to the initial thermal bound). At longer times, generalized vacuum-Rabi collapses and revivals experimentally appear, confirming the coherent nature of the many-body quantum dynamics.

Together, these observations establish ion crystals as a scalable platform for probing non-equilibrium quantum dynamics, and for experimentally bridging the gap between classical chaos and quantum thermalization via the generation of entangled states relevant for metrology and quantum information scrambling [31–41].

II. EXPERIMENTAL IMPLEMENTATION

The Dicke model has been studied in a wide range of experimental settings over the years, beginning with cavity-QED experiments using thermal gases [9, 10], and extending to implementations with Bose-Einstein condensates [8, 11–17]. Related realizations have also been achieved in circuit-QED platforms [19, 20] and exciton-polariton microcavities in solid-state systems [21]. More recently, cavities combined with optical tweezers [18, 42] have provided access to the model’s equilibrium behavior under more controllable conditions, while trapped-ion experiments [31, 43–46] have enabled clean, controllable implementations of collective spin-boson dynamics.

In this work, our quantum simulator is based on a single-layer Coulomb crystal comprising approximately $N \sim 100$ ${}^9\text{Be}^+$ ions confined within a Penning trap [46–50] (see Fig. 1a). Each ion hosts a spin-1/2 degree of freedom, $|\uparrow\rangle \equiv |m_J = +1/2\rangle$ and $|\downarrow\rangle \equiv |m_J = -1/2\rangle$, encoded in the valence electron’s ground-state ${}^2S_{1/2}$ manifold. These spin states can be coherently manipulated using microwave radiation with frequency resonantly tuned to the 124 GHz Zeeman splitting induced by a strong external magnetic field of $B = 4.46$ T.

A pair of off-resonant laser beams, with frequency difference μ and detuned by approximately 12 GHz from nearby optical transitions, form a one-dimensional traveling-wave potential that couples the axial motion to the spin degree of freedom via a spin-dependent optical dipole force (ODF). In this work, the ODF frequency μ is tuned near the axial center-of-mass (COM) mode at $\omega_Z/(2\pi) = 1.59$ MHz with frequency difference $\delta = \mu - \omega_Z$. This choice ensures that the spins selectively couple to the COM mode, while all other motional modes remain effectively unpopulated. In addition to standard Doppler cooling and in comparison to past works [46, 51], we also employ an additional pair of off-

resonant laser beams to enable further electromagnetically induced-transparency (EIT) cooling of the motional modes [52].

In the Lamb-Dicke regime, in which the axial spread of the ions is small relative to the optical wavelength of the ODF beams, this setup realizes a pristine implementation of the Dicke model [4, 31, 43], with behavior effectively described by the model Hamiltonian $\hat{H}_{\text{Dicke}} = \hat{H}_0 + \hat{H}_{\text{s-p}}$ [43, 53], where

$$\hat{H}_0/\hbar = -\delta\hat{a}^\dagger\hat{a} + \Omega\hat{S}_x \quad \hat{H}_{\text{s-p}}/\hbar = \frac{2g}{\sqrt{N}} (\hat{a} + \hat{a}^\dagger) \hat{S}_z. \quad (1)$$

Here, \hat{a} and \hat{a}^\dagger denote bosonic annihilation and creation operators for phonon excitations of the COM mode, which couple uniformly to the collective spin described by the angular momentum operators $\hat{S}_{\alpha=x,y,z} = \sum_{j=1}^N \hat{\sigma}_{\alpha,j}/2$ where $\hat{\sigma}_{\alpha,j}$ ($\alpha = x, y, z$) denote the Pauli matrices for the j th spin encoded in the $|\uparrow\rangle, |\downarrow\rangle$ states. The coupling, $g > 0$, is set by the strength of the spin-dependent optical dipole force, and the Rabi frequency Ω is determined by the amplitude of the applied microwave radiation.

III. THE DICKE MODEL PHASE DIAGRAM

Equilibrium Phases: At zero temperature ($\mathcal{T} = 0$), the Dicke model undergoes an equilibrium quantum phase transition (QPT) at a critical drive strength $\Omega_c^{(\text{QPT})} = 4g^2/|\delta|$, for $\delta < 0$ in our convention [5, 6]. For $\Omega > \Omega_c^{(\text{QPT})}$ (the “normal” phase), the ground state is characterized by spins aligned along the transverse field and an unpopulated bosonic mode. In contrast, for $\Omega < \Omega_c^{(\text{QPT})}$ (the “superradiant” phase), the system exhibits a ferromagnetic spin configuration with $\langle|\hat{S}_z|\rangle \sim N/2$, together with a macroscopic occupation of the bosonic mode. Up to $1/N$ corrections, the phase transition is well characterized by a mean field (MF) description, which neglects all forms of correlations [54].

Non-equilibrium phases: When the system is driven out of equilibrium, the dynamics can feature a rich variety of behaviors depending on the initial conditions and Hamiltonian parameters, even when restricted to the fully symmetric manifold, comprising states with total spin $S = N/2$, where $S(S+1)$ are the eigenvalues of the total spin operator $\hat{\mathbf{S}} \cdot \hat{\mathbf{S}}$ and $\hat{\mathbf{S}} = (\hat{S}_x, \hat{S}_y, \hat{S}_z)$.

We focus on two specific initial conditions:

All spins initially prepared in $|\downarrow\rangle$: When all spins are initially prepared in the collective eigenstate of $\hat{S}_z|m_z\rangle = m_z|m_z\rangle$ with $m_z = -N/2$, and the bosons in vacuum, the system features dynamical phase transitions (DPTs) or distinct dynamical behaviors separated by a critical point [55–59]. These are observable in the time-averaged MF magnetization, $\langle\hat{S}_z\rangle_{\text{avg.}} \equiv \lim_{T \rightarrow \infty} (1/T) \int_0^T dt \langle\hat{S}_z(t)\rangle$, which serves as a dynamical order parameter. In broad terms, the DPTs are

well described by a classical MF analysis, which predicts rich dynamical behaviors that range from analytically tractable regimes when the spins and bosons remain trapped or untrapped, to non-integrable regimes in which near-resonant spin-boson coupling gives rise to chaotic behavior [5, 6, 31].

More quantitatively, when $|\delta| \gg |\Omega|, |g|$ the population of bosonic excitations is energetically suppressed, and to leading order their role reduces to virtual mediators of interactions between the spins¹. In this regime, the dynamics can be described by a pure spin model known as the Lipkin-Meshkov-Glick (LMG) model [60–62], with a Hamiltonian given by

$$\hat{H}_{\text{LMG}} = \frac{\chi}{N} \hat{S}_z^2 + \Omega \hat{S}_x \quad \chi \equiv 4g^2/\delta. \quad (2)$$

This model has been widely explored experimentally, from its MF dynamical phases in the infinite range interaction limit [29, 63] to the development of non-trivial quantum correlations in the presence of power-law decaying couplings [27].

As indicated by the solid black line on the classical MF phase diagram shown in Fig. 1b, a critical drive $\Omega_c^{(\text{DPT})} = \chi/2 = \Omega_c^{(\text{QPT})}/2$, separates a dynamical ferromagnetic phase (trapped), where the instantaneous magnetization $\langle \hat{S}_z \rangle$ oscillates about a non-zero time-averaged value, remaining trapped below the equator of the Bloch sphere (Fig. 1d) with $\langle \hat{S}_z \rangle_{\text{avg.}} \neq 0$, and a dynamical paramagnetic phase (untrapped), dominated by the transverse field Ω , which leads to Rabi flopping with $\langle \hat{S}_z \rangle_{\text{avg.}} = 0$. The adiabatically eliminated bosons are bound to the motion of the collective spin, $\langle \hat{a} + \hat{a}^\dagger \rangle \propto (2g/\delta\sqrt{N})\langle \hat{S}_z \rangle$, and their dynamics reflect that of the spins (Fig. 1e), as can be seen by the corresponding loops in phase space, described by the quadratures $\hat{\mathcal{X}} = (\hat{a} + \hat{a}^\dagger)/\sqrt{2}$ and $\hat{\mathcal{P}} = i(\hat{a}^\dagger - \hat{a})/\sqrt{2}$.

However, when $|\delta|$ is decreased so that $|\delta| \sim |\Omega| \sim |g|$, the bosons play an active role in the dynamics and cannot be adiabatically eliminated [64]. In this regime, the time-averaged order parameter features more complex behavior, with typical MF time-traces featuring erratic oscillations in both spin and boson observables (see Fig. 1d,e), with short periods where the system sporadically becomes re-trapped. This behavior signals the onset of a chaotic dynamical phase [62, 65], arising due to the known non-integrability of the Dicke model [4, 6, 66, 67]. The underlying complexity can be characterized by computing the Lyapunov exponent λ_L [4] in Fig. 1c) (see also Ref. [53]) as a function of Ω/δ and $\Omega/\chi \propto \Omega\delta/g^2$.

Chaos, and thus non-integrability, is classically signaled by $\lambda_L > 0$ [68]. However, in contrast to the LMG

regime where the full quantum dynamics are well described by MF theory, in the active phonon regime quantum fluctuations can play a more significant role and lead to a rapid dephasing as the different MF trajectories diverge, washing out these erratic oscillations [31].

All spins initially prepared parallel and opposite to the drive orientation: Genuine quantum behaviors emerge in the Dicke model when the initial spin state is $|(-N/2)_x\rangle$, and the bosonic mode has no first-order coherence, namely $\langle \hat{\mathcal{X}} \rangle, \langle \hat{\mathcal{P}} \rangle = 0$. This initial state is a fixed stationary point of the MF dynamics (see inset of Fig. 1f). For such initial conditions, non-trivial dynamics are only driven by thermal or quantum fluctuations away from the stationary point. Thus, for an initial bosonic vacuum, quantum noise is the sole driver of dynamics, requiring the use of beyond MF methods to model the resulting behavior, such as the truncated Wigner-approximation (TWA [69], see [53]). In Fig. 1, we show TWA dynamics of the time average transverse order parameter, $\langle \hat{S}_x \rangle_{\text{avg.}}$, which displays non trivial behavior in a narrow region about $\Omega/\delta \sim 1$.

To elucidate the underlying physics, it is useful to consider the joint rotating frame of the transverse drive and bosonic field, \hat{H}_0 , where the interaction frame Hamiltonian can be written as $\hat{H}_{\text{s-p}}^{\text{rot}} = \hat{H}_{\text{pair}}^{\text{rot}} + \hat{H}_{\text{osc}}^{\text{rot}}$ for

$$\hat{H}_{\text{pair}}^{\text{rot}}/\hbar \equiv \frac{-ig}{\sqrt{N}} \left(\hat{a}^\dagger \hat{S}_+^{(x)} e^{i(\Omega-\delta)t} - \hat{a} \hat{S}_-^{(x)} e^{-i(\Omega-\delta)t} \right), \quad (3)$$

$$\hat{H}_{\text{osc}}^{\text{rot}}/\hbar \equiv \frac{-ig}{\sqrt{N}} \left(\hat{a} \hat{S}_+^{(x)} e^{i(\Omega+\delta)t} - \hat{a}^\dagger \hat{S}_-^{(x)} e^{-i(\Omega+\delta)t} \right), \quad (4)$$

where we have defined spin ladder operators in the x basis via $\hat{S}_y \equiv (\hat{S}_+^{(x)} + \hat{S}_-^{(x)})/2$ and $\hat{S}_z \equiv (\hat{S}_+^{(x)} - \hat{S}_-^{(x)})/(2i)$.

When $\delta = \Omega$ and $|\delta| \gg g$, $\hat{H}_{\text{osc}}^{\text{rot}}$ rapidly oscillates and can be ignored. The dynamics are then governed by the static term $\hat{H}_{\text{pair}}^{\text{rot}}$, which generates correlated spin-boson excitations. This behavior can be easily understood by using the so called Holstein-Primakoff (HP) approximation [70], which maps spin operators into bosonic operators \hat{b} . In the large N limit, and for an initial state polarized along $-x$, the HP approximation simplifies to $\hat{S}_+^{(x)} \approx \sqrt{N}\hat{b}^\dagger$ and $\hat{S}_x = -N/2 + \hat{b}^\dagger\hat{b}$. In terms of the bosonic modes, $\hat{H}_{\text{pair}}^{\text{rot}}/\hbar \approx -ig(\hat{a}^\dagger\hat{b}^\dagger - \hat{a}\hat{b})$, which is an iconic two-mode squeezing Hamiltonian (studied in a broad range of experimental settings [71–84], see also Ref. [53]). As schematically shown in Fig. 1(f,g), in a two-mode squeezing model, excitations are generated through correlated pair-creation processes that simultaneously populate both modes. As a result, excitations are not produced independently but emerge as entangled pairs with strongly correlated occupations. This cooperative generation leads to exponential growth of mode populations from vacuum, $\langle \hat{a}^\dagger\hat{a} \rangle = \langle \hat{b}^\dagger\hat{b} \rangle \sim \langle \hat{S}_x + N/2 \rangle \sim \sinh^2(gt)$. Furthermore, it produces non-classical correlations in the form of reduced (squeezed) fluctuations along two independent, hybrid quadrature operators [85]— $\hat{V}_+ \equiv$

¹ For all our results, we take $g, \Omega, \delta > 0$. For our z -polarized initial state, however, we note that the dynamics of $\langle \hat{S}_z \rangle$ do not depend on the relative sign of δ , and—in the ideal case—also do not depend on the signs of g and Ω .

$\hat{P} + \hat{S}_z/\sqrt{N/2}$ and $\hat{W}_+ \equiv \hat{X} + \hat{S}_y/\sqrt{N/2}$ —and enhanced fluctuations (antisqueezing) along the remaining two conjugate quadratures— $\hat{V}_- \equiv \hat{P} - \hat{S}_z/\sqrt{N/2}$ and $\hat{W}_- \equiv \hat{X} - \hat{S}_y/\sqrt{N/2}$ [53]. At longer times, after the build-up of many excitations, the $1/N$ corrections neglected in the HP approximation become relevant. Here, instead of continuous growth of excitations, dynamics undergo collapses and revivals, akin to vacuum oscillations in the Rabi model, but with non-sinusoidal oscillations and characteristic damping owing to the comparatively complex spectrum of the Dicke model.

Away from the regime $|\delta| \gg g$, when $\delta = \Omega$, it is necessary to retain the previously neglected oscillatory terms $\hat{H}_{\text{osc}}^{\text{rot}}$. Their inclusion leads to the onset of chaos and thermalization. In this case, thermalization dynamics in a closed quantum system can be characterized through the Rényi entropy. For the reduced density matrix of a single spin, the second-order Rényi entropy is given by

$$S_2(\hat{\rho}_j) = -\log_2[\text{Tr}(\hat{\rho}_j^2)] = -\log_2 \left[\frac{1}{2} + \frac{2\langle \hat{S}_x \rangle^2}{N^2} \right], \quad (5)$$

where $\hat{\rho}_j$ is the reduced density matrix for the single spin labeled by j . In Eq. 5, we assumed an x -polarized initial condition, and considered the symmetry of \hat{H}_{Dicke} enforcing $\langle \hat{\sigma}_{y,j} \rangle = \langle \hat{\sigma}_{z,j} \rangle = 0$ as well as $\langle \hat{\sigma}_j \rangle = 2\langle \hat{S}_j \rangle/N$. A finite Rényi entropy, $S_2(\hat{\rho}_j) > 0$, is a direct measure of entanglement in a global pure state [86].

IV. PROBING THE LMG DYNAMICAL PHASE DIAGRAM

In our system, we first explore the integrable spin limit of the Dicke model by tuning to a regime where $|\delta| \gg |g|, |\Omega|$, where the phonons may be adiabatically eliminated from the system and the dynamics are well described by the LMG model in Eq. (2). We can identically prepare the spins in the $|\downarrow\rangle$ state and, via Doppler cooling, obtain a Doppler-limited thermal occupation of $\bar{n} \sim 5$ for the COM mode. We can achieve $\bar{n} \lesssim 1$ via electromagnetically induced transparency (EIT) cooling, heavily mitigating thermal effects in the resulting dynamics. We also note that in the experiment, the typical spin-spin interaction rate, χ , is much larger than the single-particle spin decoherence rate, Γ , arising from scattering processes induced by the ODF beams; we thus have the hierarchies $|\delta| \gg |g|, |\Omega|$, and $|\chi|, |\Omega| \gg \Gamma$.

We prepare the state described by the density operator $\hat{\rho}_z = \hat{\rho}_{\text{th}} \otimes |(-N/2)_z\rangle \langle (-N/2)_z|$, where $\hat{\rho}_{\text{th}}$ is the appropriate thermal state of the phonons corresponding to our cooling scheme. We then let the system evolve in the presence of both the ODF and the resonant transverse microwave field, for variable time $t \leq T = 3$ ms. After the desired time evolution, we turn off both ODF lasers and microwaves and perform a fluorescence measurement of the spin populations, yielding information

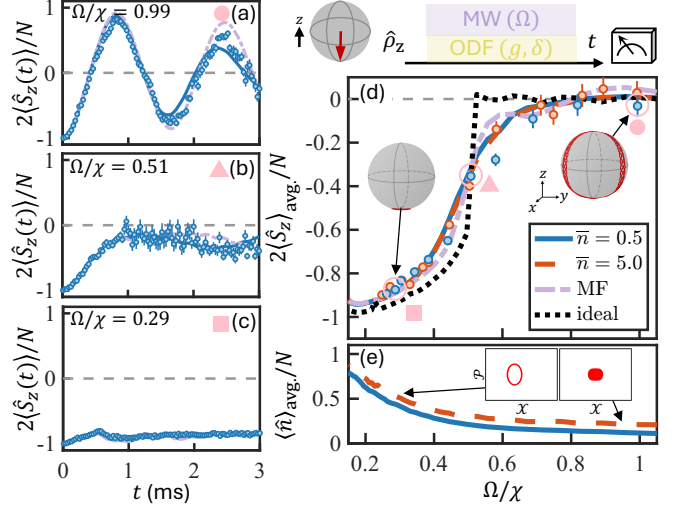


FIG. 2. Dynamical phase transition in the integrable, spin-dominated limit (see pink “LMG cut” in Fig. 1 and corresponding pink symbols). (a-c) Representative time traces of $2\langle \hat{S}_z(t) \rangle/N$ for initial EIT-cooled phonons and $-z$ polarized spins, following a variable time pulse of the ODF beams and MW source to simulate an LMG model (see sketch, top right). We compare against semiclassical (blue-solid) and mean-field (MF) models (lavender-dashed-dot), including relevant experimental details. (d) Magnetization averaged over 3 ms of evolution for initial EIT (blue, $N \in [86, 167]$) and Doppler (orange, $N \in [57, 79]$) cooling, compared to semiclassical (blue solid, $\bar{n} = 0.5$; orange-dashed, $\bar{n} = 5.0$) and MF (lavender dashed-dot) results with $N = 100$; idealized MF results are also shown (black dotted), averaged over $0 - 20$ ms. (e) We also present corresponding semiclassical predictions for the time-averaged phonon occupancy, not directly accessible in the experiment. Bloch sphere/phase space schematics next to pink symbols correspond to the parameters and behaviors outlined in Fig. 1b-e. $\Omega/\delta \in [0.12, 0.13]$ and $g \in 2\pi \times [0.93, 1.00]$ kHz throughout. Error bars denote standard-error of the mean.

regarding $|m_z\rangle$ (see Ref. [53]).

In Fig. 2a-c we present time traces at fixed $\Omega/\delta \sim 0.1$ and $g \sim 2\pi \times 0.9$ kHz, while varying the value of $\Omega/\chi = \Omega\delta/4g^2$ for $\Omega, \delta > 0$ (see pink line in Fig. 1b). At small Ω/χ , Fig. 2c, we observe that the magnetization remains close to its initial value, undergoing small oscillations as the Bloch vector remains trapped below the equator by the interaction-induced self-precession. This behavior is summarized in Fig. 2d, which shows the time-averaged magnetization order parameter up to $T = 3$ ms, as a function of Ω/χ . The order parameter remains well below the equator for $\Omega < \Omega_c^{(\text{DPT})}$. At $\Omega > \Omega_c^{(\text{DPT})}$ we observe a sudden saturation of the time-average magnetization of $\langle \hat{S}_z \rangle_{\text{avg}}$ to 0, as the typical dynamics undergo unconstrained Rabi oscillations shown in Fig. 2a. We compare the experimental dynamics and resulting mean magnetization to a semiclassical model without free parameters, based on the TWA that accounts for relevant experimental decoherence sources including measured light scatter-

ing, magnetic field noise, and thermal occupation of the phonons [53]. We also compare both the time traces and mean magnetization against a classical MF model (lavender dashed-dot line), which does not incorporate effects of thermal and quantum fluctuations in the initial state, and also neglects the build-up of classical correlations from stochastic noise sources. In all cases, we observe that both the TWA and the MF model provide excellent agreement with our data, validating the MF nature of the DPT.

The fact that both Doppler-limited cooling and EIT cooling schemes feature similar dynamics in the LMG limit further confirms the passive role played by the phonons. While not directly accessible in the experiment, in Fig. 2e, we show the time averaged phonon population, $\langle \hat{n} \rangle_{\text{avg}} \equiv \lim_{T \rightarrow \infty} (1/T) \int_0^T \langle \hat{n}(t) \rangle dt$ for phonon occupation operator $\hat{n} \equiv \hat{a}^\dagger \hat{a}$, computed from our TWA simulations. The mean phonon occupation is qualitatively similar for different initial phonon occupations, though the hotter initial phonon distribution leads to a consistently higher time-averaged occupation. As the spins become increasingly trapped, the mean phonon population increases, reflecting the increased rate of mediated spin-spin interactions and highlighting the fact that phonon dynamics are locked to the spins.

We also observe the critical point close to $\Omega_c^{(\text{DPT})}$ [29], but instead of the expected sharp behavior, we observe a slightly smoother transition, consistent with the finite extent of the evolution time T . The smoother transition is, however, not a consequence of finite N , which differs for the two initial phonon configurations: $N \sim 57 - 79$ and $86 - 167$ for the hotter and colder cases, respectively. To emphasize this point we show the ideal MF dynamics (black dashed line), computed for $N = 100$ and averaged up to $T = 20$ ms. The longer averaging time clearly gives rise to a non-analyticity at the transition.

V. EXPLORING CHAOTIC DICKE DYNAMICS

To explore the transition from regular to chaotic dynamics, we experimentally probe the regime where phonons can play an active role. We accomplish this by varying the ratio Ω/δ while keeping $\Omega/\chi \sim 0.4$ and $g \sim 2\pi \times 1.1$ kHz fixed (see green line in Fig. 1b), utilizing the same initial conditions described in Fig. 2. In Fig. 3a-c, we show characteristic time traces for the spin evolution. Regular dynamics are observed for both small $|\Omega|, |g| \ll |\delta|$, where the system once again lies in the dynamical ferromagnetic phase of the LMG model, and for large $|\Omega| \gg |g|, |\delta|$, where the role of the spins and the phonons are reversed, with the spin precession bound to the mean phonon occupation. This amounts to Rabi flopping about zero mean magnetization.

In the intervening regime, however, neither $|\Omega|$ nor $|\delta|$ are sufficiently large to energetically suppress the spin-boson coupling. Classically, this results in chaotic, non-

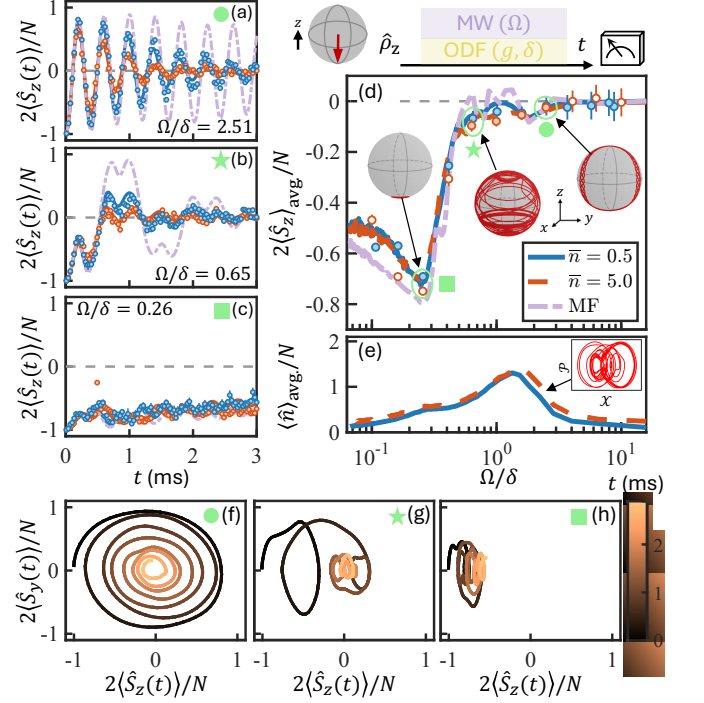


FIG. 3. Non-integrable dynamics and chaos in the Dicke model (see green cut and corresponding symbols in Fig. 1). (a-c) Representative spin dynamics for initial EIT (blue) and Doppler (orange) cooling and $-z$ polarized spins, following an analogous sequence to Fig. 2 to simulate the Dicke model (see also sketch, top right), compared against semiclassical (blue/orange solid) and MF models (lavender dashed-dot), including relevant experimental details. (d) Magnetization averaged over 3 ms of evolution, with filled (unfilled) symbols corresponding to results with $N \in [51, 108]$ ($N \in [159, 178]$). We compare to semiclassical (blue solid, $\bar{n} = 0.5$; orange dashed, $\bar{n} = 5.0$) and MF (lavender dashed-dot) results with $N = 100$, (e) and also show the semiclassically predicted time-averaged phonon occupancy. Bloch sphere and phase space diagrams associated with green symbols display typical classical behaviors and corresponding parameters outline in Fig. 1b-e. (f-h) Experimental phase space dynamics corresponding to (a-c) of the mean magnetization (with EIT-cooled initial phonons), with color denoting the elapsed time. $\langle \hat{S}_y(t) \rangle$ is computed from the time-derivative of smoothed dynamics, see Ref. [53] for details. $\Omega/\chi \in [0.41, 0.47]$ and $g \in 2\pi \times [1.07, 1.15]$ kHz throughout (for unfilled symbols, $g \approx 2\pi \times 0.88$ kHz). Error bars denote standard-error of the mean.

integrable dynamics, expected from the nonzero Lyapunov exponent in Fig. 1c, which replaces the smooth circular orbits in phase space, to irregular, erratic trajectories that jump between the different trapped points. Examples of such erratic trajectories can be seen in the $\langle \hat{S}_y \rangle$ vs $\langle \hat{S}_z \rangle$ phase space plane shown in Fig. 3f-h. Experimentally, $\langle \hat{S}_y \rangle$ is not directly measured but extracted from the time derivative of the $\langle \hat{S}_z \rangle$ time traces. The experimental traces are in full agreement with theoretical TWA dynamics, which are shown in Ref. [53].

Significant discrepancies between the MF predictions

and the experimental observations emerge in the chaotic regime (Fig. 3b), and the neighboring regions (Fig. 3a), even when accounting for relevant technical noise sources. Here, fluctuations in the initial phonon distribution give rise to a strong damping of the spin magnetization dynamics, even with EIT cooling where the initial thermal phonon occupation is minimized. The time traces with Doppler-limited cooling exhibit larger damping, attributable to the enhanced thermal fluctuations in the phonons. These results, as supported by the agreement with the TWA simulations in both cases (see also Fig. (10) in Ref [53]), highlight the genuine role played by quantum vacuum fluctuations, which drive beyond MF effects.

Interestingly, the differences in the transient dynamics featured by the two initial phonon distributions essentially vanish in the time-averaged magnetization, shown in Fig. 3d, a feature also captured by the TWA dynamics; these results also resemble the time-averaged MF dynamics. Nonetheless, even in the presence of native decoherence in the experiment, we predict the generation of large spin-phonon excitations in this chaotic region. This is reflected in the large peak exhibited by the theoretical predicted time-average phonon population in Fig. 3e.

VI. RESONANT DYNAMICS: EXPONENTIAL GROWTH, PAIR PRODUCTION AND ENTANGLEMENT

To further illuminate the onset of genuine quantum effects and non-integrable dynamics in the Dicke model, we explore the dynamics when the initial spin state is instead polarized along the x direction. We plot time traces of the transverse magnetization $\langle \hat{S}_x(t) \rangle$ —accessed by an additional $\pi/2$ -pulse before fluorescence measurements of the spin population—in Fig. 4, taken through the orange cut shown in Fig. 1. For these measurements, we restrict to initial states prepared with EIT cooling (blue circles), and our results are again validated by the numerical TWA dynamics (blue line).

All time traces shown in Fig. 4a-c feature growth of quantum-mechanically driven correlated spin-boson excitations at short times, which is fully consistent with the ideal exponential growth shown by the green dotted line. Nevertheless, at longer times there is a distinct change in behavior. In the small $\Omega/\chi = \delta^2/(4g^2) < 1$ limit, the x magnetization quickly thermalizes, signaling the emergence of non-integrable chaotic dynamics induced by the spin-boson entanglement and the fast buildup of bosonic excitations. On the contrary, in the regime $\Omega/\chi = \delta^2/(4g^2) > 1$, we clearly see the expected collapses and revivals at longer times, emerging from the more constrained growth of correlated spin-boson excitations. These can be understood as archetypal *vacuum* Rabi oscillations in the Tavis-Cummings model [87], which can serve as a direct indicator of squeezed correlations in the system.

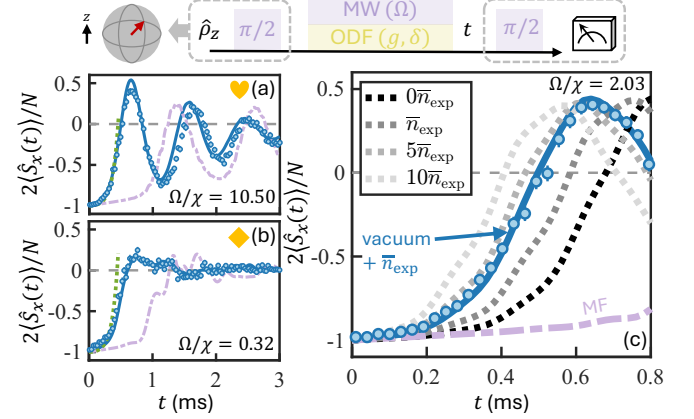


FIG. 4. Fluctuation-driven, unstable fixed-point dynamics in the resonant spin-phonon regime (see orange trace Fig. 1f, and corresponding orange symbols). (a-b) Representative transverse spin dynamics for initial EIT-cooled phonons and $-x$ polarized spins, using a modification of the pulse sequence in Fig. 2 to prepare and access the transverse magnetization (see sketch, top). We compare against our semiclassical (blue-solid) and MF models (lavender dashed-dot), including relevant experimental details, as well as analytic results from a large- N expansion (green dotted). (c) We also compare to a classical model accounting for classical correlations from different noise sources, with different levels of added initial thermal noise in the phonons, quantified as multiples of measured occupancy $\bar{n}_{\text{exp}} \sim 0.5(2)$. $\Omega/\delta \in [0.89, 1.02]$ and $g \in 2\pi \times [0.87, 0.91]$ kHz throughout, and $N \in [89, 112]$. Error bars denote standard-error of the mean.

While the ideal MF solution exhibits no dynamics (see inset of Fig. 1f), relevant sources of decoherence and thermal fluctuations—even at the coldest temperatures accessible in the experiment—can drive dynamics away from the classically unstable fixed point. Nevertheless, we still observe marked differences between our MF solution—including technical noise at the MF level—and the full quantum dynamics. This is demonstrated in the time traces of the x magnetization shown in Fig. 4c. Furthermore, properly accounting for classical correlations from thermal noise and stochastic noise sources in our MF model (gray dotted lines) reproduces the observed dynamics *only* if the initial thermal population is artificially increased by a factor of five relative to experimental conditions. We therefore interpret the faster-than-classical evolution in the experiment as being seeded by intrinsically quantum fluctuations, namely phonon vacuum noise together with spin projection noise, which accelerate the escape from the unstable fixed point.

The time-averaged magnetization trends closer to 0 with decreasing Ω/χ , consistent with entanglement growth in the chaotic regime, as shown in Fig 5a. Characterizing entanglement in open many-body systems is notoriously challenging, since environmental coupling obscures direct entanglement measures. Here, however, we identify a parameter regime in which the collective magnetization closely follows the ideal unitary dy-

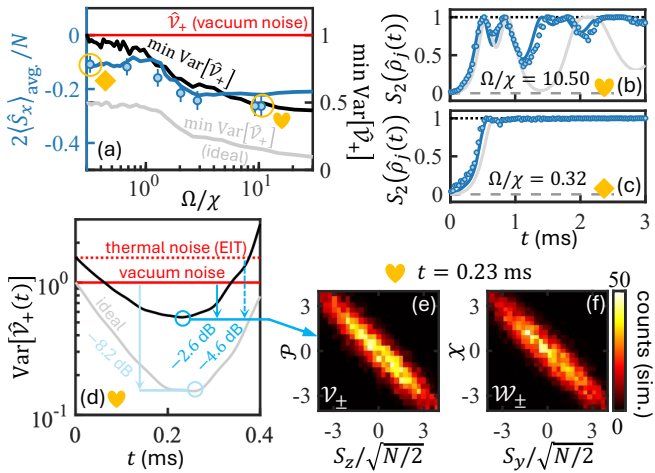


FIG. 5. Pair production and entanglement in the resonant spin-phonon regime. (a) Time-averaged transverse magnetization from results in Fig. 4, compared to our semiclassical model (blue solid). Error bars denote standard-error of the mean. (b-c) Representative dynamics of the single-qubit Rényi entropy, compared to our semiclassical model (blue solid). Maximum entropy indicated by black dotted line. (d) Simulated dynamics of composite \mathcal{V}_+ quadrature (ideal results in gray), showing noise reduction relative to the vacuum state and also the initial EIT-cooled thermal state. We also plot the corresponding minimum achieved variance \mathcal{V}_+ versus Ω/χ in panel (a); reference value for an uncorrelated vacuum phonon state displayed in red. (e-f) Semiclassical prediction for joint spin-phonon quadrature histograms, simulating 5×10^3 measurements.

namics even when unavoidable non-unitary decoherence sources are included in the simulations (see gray line, Fig. 5c). In this regime, the collective magnetization provides a direct quantitative proxy for entanglement, given that it reduces to the single-spin Rényi entropy (see Eq. (5)). This remarkable robustness allows us to interpret the experimentally measured decay of the collective x -magnetization to zero, when the single-spin Rényi entropy in Fig. 5(c) reaches its maximum value, as a direct indicator of entanglement buildup and quantum thermalization in the chaotic regime.

In contrast, such a conclusion cannot be drawn in the semi-integrable regime (Fig 5b), where the ideal collective magnetization continues to exhibit collapses and revivals, which are noticeably damped by decoherence in the experiment. In this regime, the inferred variance of the hybrid quadratures provides an alternative way to quantify entanglement, at least over short timescales. In Fig. 5a we show the theoretically expected minimal variance of the hybrid quadrature \mathcal{V}_+ , which decreases with increasing $\Omega/\chi = \delta^2/(2g)^2$ (for $\Omega = \delta$). At $\Omega/\chi = 10.50$, as shown in Figure 5d, the variance in the ideal case evolves to a minimum of approximately 1/7 of its initial value, corresponding to ~ 8.2 dB below the standard quantum limit (SQL). When decoherence is accounted for, the reduction remains significant at about ~ 2.6 dB

below SQL, corresponding to a net decrease of ~ 4.6 dB relative to the initial thermal noise.

Figures 5e,f display simulated histograms of the hybrid spin-boson phase-space quadratures, $\hat{\mathcal{V}}_{\pm}$ and $\hat{\mathcal{W}}_{\pm}$, respectively, at the optimal squeezing time for $\Omega/\chi = 10.50$. While the squeezing is inferred from numerical modeling rather than directly measured, the excellent agreement between theory and experiment points to a clear path toward implementing quantum-enhanced sensing in this system.

VII. CONCLUSION

We have realized the Dicke model in a closed quantum system comprised of a two-dimensional ion crystal, and observed dynamical phase transitions in the integrable regime and beyond MF physics driven by quantum fluctuations when both spin and phonon excitations interplay. We observed exponential growth of correlated excitations, as well as dynamics consistent with two-mode squeezing and an inferred variance reduction below the standard quantum limit at short times. At longer times, we observed collapses and revivals of oscillations, with entanglement growth inferred from the single spin Rényi entropy in the chaotic regime.

Beyond its immediate relevance for quantum metrology and for probing fundamental aspects of quantum mechanics—such as Einstein-Podolsky-Rosen (EPR) correlations and steering [88, 89], the presented observations also connect to ideas from high-energy physics and quantum information. In particular, correlated pair production has been linked to thermo-field double states [90–92], which play a central role in holography and have also appeared in discussions of quantum teleportation [93] and Hayden-Preskill-type information-recovery protocols [34]. Over all, our work establishes large two-dimensional ion arrays as a platform for exploring how entanglement, chaos, and holographic concepts can be harnessed for quantum technologies in experimentally accessible, many-body systems.

ACKNOWLEDGMENTS

We thank Diego Fallas Padilla and Kurt A. Thompson for excellent feedback on the manuscript, and Diego Barberena and Justin Bohnet for useful discussions. This work was supported by ARO W911NF24-1-0128, AFOSR FA9550-25-1-0080, the NSF JILA-PFC PHY-2317149, the NSF JILA-PFC PHY-2317149, The Heising-Simons Foundation and the U.S. Department of Energy, Office of Science, National Quantum Information Science Research Centers, Quantum Systems Accelerator, and NIST. S.R.M. is supported by the NSF QLCI award OMA-2120757. A.S.N. is supported by the Dutch Research Council (NWO/OCW) as a part of the Quantum Software Consortium (project number 024.003.037).

Appendix A: Experimental details

Here we provide a more detailed description of the experimental ion trap set-up used to realize the Dicke model along with a discussion of the experimental protocols employed for controlling and measuring the relevant model parameters.

Crystals of ${}^9\text{Be}^+$ ions are confined in a room-temperature Penning ion trap and formed through Doppler laser cooling. The trap consists of cylindrical electrodes that are used to generate a deep, harmonic confining potential along the axis of the cylinders, denoted by the Z -axis of the trap. The trap resides in the bore of a 4.46 T superconducting magnet with the Z -axis of the trap aligned with the magnetic field direction to better than a few hundredths of a degree [94, 95]. Radial confinement of the ions is obtained from the Lorentz force due to $\mathbf{E} \times \mathbf{B}$ induced rotation of the ion crystal at a frequency ω_r . The ion crystal rotation frequency ω_r is precisely controlled with a rotating electric potential, dubbed the rotating wall potential [96]. In a frame rotating at ω_r , the effective confining potential of the trap, ignoring the weak rotating wall potential, is well approximated by

$$q\phi_{\text{trap}}(\rho, Z) = \frac{1}{2}M\omega_Z^2(Z^2 + \beta\rho^2), \quad (\text{A1})$$

where q is the ion charge, M is the ion mass, and Z and ρ are the respective axial and radial distance from trap center. $\omega_Z/(2\pi) \approx 1.59$ MHz characterizes the ion confinement along the axial or magnetic field direction, and $\beta = \omega_r(\Omega_c - \omega_r)/\omega_Z^2 - 1/2$ is the relative strength of the radial confinement for rotation frequency ω_r and cyclotron frequency Ω_c . For the work discussed here, $\Omega_c/2\pi = 7.6$ MHz and the rotation frequency was set to $\omega_r/2\pi \approx 180$ kHz, resulting in $\beta \approx 0.026$ and single plane crystals for ion number $N \lesssim 500$ ions.

In the strong 4.46 T magnetic field of the Penning trap, the ${}^9\text{Be}^+$ atomic eigenstates are approximately described by product states $|m_I\rangle |m_J\rangle$ of the $I = 3/2$ nuclear spin and valence electron angular momentum J quantum numbers. The nuclear spin is optically pumped to the $|m_I = 3/2\rangle$ level, where it remains throughout the experiment, simplifying the relevant energy level structure shown in Fig. 6. The spin-1/2 or qubit degree of freedom in each ion consists of the ground valence electron spin states $|\uparrow\rangle \equiv |2S_{1/2} m_j = 1/2\rangle$ and $|\downarrow\rangle \equiv |2S_{1/2} m_j = -1/2\rangle$. These levels are separated by approximately 124 GHz by the magnetic field. A low phase noise microwave source [97] at 124 GHz enables coherent global rotations of the ion qubits and implementation of the transverse field interaction of the Dicke model with Rabi rates as large as $\Omega/2\pi \approx 5.7$ kHz. A voltage controlled attenuator allows tuning Ω arbitrarily below this maximum.

Doppler cooling and state-selective read-out is performed on the cycling transition

$|\uparrow\rangle \rightarrow |^2P_{3/2} m_J = +3/2\rangle$. During cooling, laser beams directed parallel and perpendicular to the magnetic field are tuned $\approx 10\text{-}20$ MHz below the $|\uparrow\rangle \rightarrow |^2P_{3/2} m_J = +3/2\rangle$ cycling transition frequency. For spin state detection, photons are collected on a photomultiplier tube (PMT) from the global fluorescence of ions in the $|\uparrow\rangle$ state using only the parallel beam detuned ≈ 1 MHz below the cycling transition resonance. The PMT counts are integrated over roughly 0.5 ms to give roughly 2 photons per bright ion, chosen based on the trade-off between reducing photon shot noise and limiting in-plane heating. Qubit state initialization is performed with optical pumping into the $|\uparrow\rangle$ state using the Doppler cooling lasers and a repump laser tuned to the $|\downarrow\rangle \rightarrow |^2P_{3/2} m_J = +1/2\rangle$ transition frequency. We also observe ion fluorescence using a camera that records both the timing and position information of photon arrivals. This information can be used in postprocessing to obtain an image in the rotating frame, as shown in Fig. 7. These images allow us to count the number of ions N directly. We can also use these images to obtain a more accurate estimate of the average photons per ion recorded in 1 ms to improve the calibration of N without images.

Ion motion parallel to the magnetic field can be described in terms of a set of normal modes frequently called the drumhead modes [98]. The highest frequency drumhead mode is the axial center-of-mass (COM) mode, consisting of an in-phase, uniform oscillation of all the ions in the crystal at the trap frequency ω_Z . The Q factor of the COM mode has been measured to be $Q > 10^6$ through a ring down measurement [95]. The drumhead modes are efficiently cooled by the Doppler laser cooling beams. Measurements of the ion temperature for motion parallel to the magnetic field are consistent with the 0.4 mK Doppler laser cooling limit for ${}^9\text{Be}^+$ [52]. For the $\omega_Z/2\pi = 1.59$ MHz axial center-of-mass (COM) mode, this corresponds to a mean phonon occupation number of $\bar{n} \approx 4.6$. For $N \lesssim 150$, the axial COM mode is separated from the next highest frequency drumhead modes (the so-called tilt modes) by greater than 20 kHz.

The temperature of the drumhead modes can be reduced further through electromagnetically induced transparency (EIT) cooling [52, 99]. We implement EIT cooling by coherently coupling the two qubit levels to the same $|^2P_{3/2} m_J = 1/2\rangle$ excited state through two different laser beams as shown in Fig. 6. The beams are tuned to a virtual level approximately 400 MHz to the high frequency side of the $|^2P_{3/2} m_J = 1/2\rangle$ level. The two EIT laser cooling beams intersect the ion crystal at ± 10 degree angles with respect to the crystal plane, producing a wave vector difference $\Delta\mathbf{k}$ that is aligned with the magnetic field axis (Z -axis) of the trap (see Fig. 1a). Fine tuning of the EIT laser cooling parameters generates enhanced scattering on the motion subtracting versus the motion adding sidebands, while a dark state completely suppresses carrier transitions, resulting in lower motional temperatures. EIT cooling reduces the temperature of

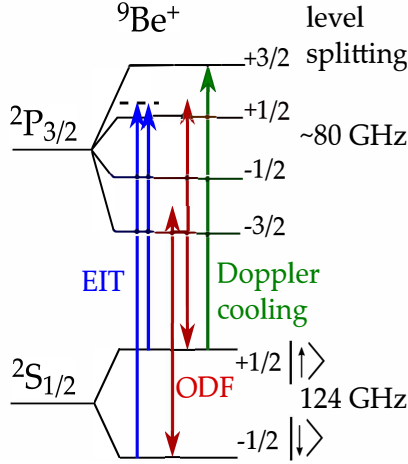


FIG. 6. ${}^9\text{Be}^+$ energy level diagram with corresponding laser frequencies.

the entire spectrum of drumhead modes with a measured temperature of the axial COM mode of $\bar{n} \lesssim 0.5$. We note that, for the work discussed here, ion motion in the plane of the ion crystal was only Doppler cooled, resulting in higher temperatures than for motion parallel to the magnetic field [98, 100].

The axial COM mode is coupled to the spin degree of freedom through the application of a spin-dependent optical dipole force (ODF). Two laser beams, tuned within the ${}^2\text{P}_{3/2}$ manifold but off resonance with any optical transitions by approximately 12 GHz (see Fig. 6), intersect the ion crystal at ± 10 degree angles with respect to the crystal plane (see Fig. 1), forming a 1-dimensional (1D) optical lattice with a wavelength of approximately 0.9 μm . The wavefronts of the 1D lattice are aligned to be parallel with the ion crystal plane. In addition, the frequency ω_{ODF} and polarizations of the ODF laser beams are tuned to values that null the AC Stark shift (ACSS) from each individual beam but generate a spin-dependent force from the interference of the beams with the force on $|\uparrow\rangle$ equal in magnitude but opposite in sign to the force on $|\downarrow\rangle$ [47, 51, 94]. In the Lamb Dicke approximation, the ODF interaction can be written as

$$\hat{H}_{\text{ODF}} = F_0 \cos(\mu t) \sum_{j=1}^N \hat{Z}_j \hat{\sigma}_j^z, \quad (\text{A2})$$

where F_0 is the magnitude of the spin-dependent force, μ is the frequency difference between the two ODF laser beams, and \hat{Z}_j is the axial position operator for the j^{th} ion,

$$\hat{Z}_j = \sum_{m=1}^N b_{j,m} \sqrt{\frac{\hbar}{2M\omega_m}} (\hat{a}_m e^{-i\omega_m t} + \hat{a}_m^\dagger e^{i\omega_m t}). \quad (\text{A3})$$

Here we use an interaction picture with respect to the free drumhead mode frequencies ω_m . The sum is over

all drumhead modes m with frequency ω_m , raising and lowering operators \hat{a}_m^\dagger and \hat{a}_m , and participation $b_{j,m}$ of ion j . With the assumption that $\delta \equiv \mu - \omega_Z \ll \mu - \omega_m$ for any other drumhead mode m , H_{ODF} is approximately given by

$$\hat{H}_{\text{ODF}} \approx \frac{F_0 Z_0}{\sqrt{N}} (\hat{a} e^{i(\mu - \omega_Z)t} + \hat{a}^\dagger e^{-i(\mu - \omega_Z)t}) \sum_{j=1}^N \frac{\hat{\sigma}_j^z}{2} \quad (\text{A4})$$

where $Z_0 \equiv \sqrt{\hbar/(2M\omega_Z)}$ is the axial ground state wavefunction size for a single ion and \hat{a} and \hat{a}^\dagger now refer to the axial COM mode raising and lowering operators. After a unitary transformation we obtain

$$\hat{H}_{\text{ODF}} \approx \hbar \frac{2g}{\sqrt{N}} (\hat{a} + \hat{a}^\dagger) \hat{S}_z - \hbar \delta \hat{a}^\dagger \hat{a} \quad (\text{A5})$$

where $g \equiv F_0 Z_0 / 2\hbar$ and $\delta = \mu - \omega_Z$. Calibration of the strength g is done measuring a MF spin precession as described in [51, 94, 95].

For a single trapped ion, the ground state wavefunction size is $Z_0 \approx 19 \text{ nm}$, producing a Lamb-Dicke parameter $\eta \equiv \delta k Z_0 = 0.13$ for the optical dipole force interaction with the axial COM mode. Here $\delta k \equiv 2\pi/(900 \text{ nm})$, where 900 nm is the wavelength of the 1D optical lattice. The Lamb Dicke approximation requires

$$\delta k Z_{\text{rms},j} \ll 1 \quad (\text{A6})$$

for all ions j in the array, where $Z_{\text{rms},j} \equiv \sqrt{\langle Z_j^2 \rangle}$. For Doppler laser cooling to the 0.5 mK limit, $\delta k Z_{\text{rms},j} \approx 0.52$ for typical ion arrays used in this work. With EIT cooling to $\bar{n}_{\text{exp}} = 0.5$, $\delta k Z_{\text{rms},j} \approx 0.22$. The strength of the spin dependent force F_0 is reduced with increasing $\delta k Z_{\text{rms},j}$ by the Debye-Waller factor [101]. The MF spin precession calibration of the Dicke model parameter g measures the effective spin-dependent force, which includes the Debye-Waller factor.

Before carrying out a set of experiments, calibrations of all relevant experimental parameters are taken. These include the Hamiltonian parameters g [51] and Ω . We also measure \bar{n} [102], the quasi-static COM mode frequency fluctuations [32], the ODF laser beam polarizations that null each beam's AC Stark shift, the spin decoherence rate from magnetic field noise, and the spin decoherence rate from the application of the ODF beams, which is dominantly from off-resonant light scatter [94, 103]. The calibrations and measurements of the experimental noise and decoherence are used with TWA simulations to model non-ideal behavior of the experimental system (see the next section).

In addition to these calibrations, active tracking of the qubit (or spin-flip) frequency and the axial COM frequency are interleaved during a scan [94]. To track the qubit frequency, a Ramsey measurement with a 1 ms free precession period is carried out for three different microwave frequencies. The center frequency results in

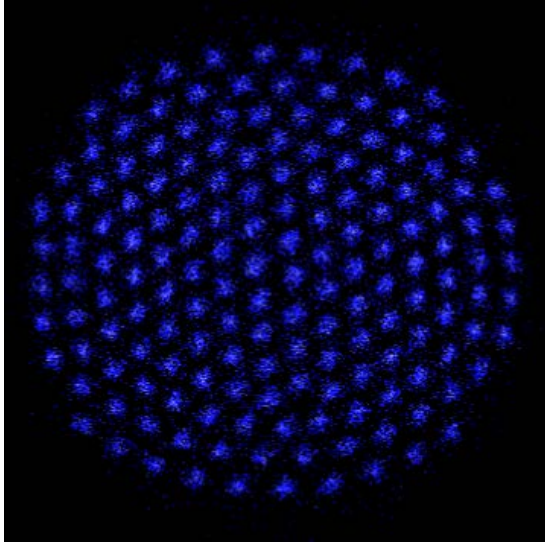


FIG. 7. Image of an ion crystal with $N = 161$ in the rotating frame.

a dip in the bright fraction near resonance, while imbalances in the measured population at the points of steepest slope on the sides of the central Ramsey fringe, called the left and right points, measure drifts in the qubit frequency. The population imbalance at the two side fringes is scaled by the fringe width and a user-adjustable gain to actively track the qubit frequency and apply appropriate shifts to the applied microwave frequency. Similarly, a resonance feature is used to track the axial COM mode and stabilize the parameter δ by adjusting the detuning between the ODF beams μ . Here the resonance feature was generated by driving with an oscillating axial electric field for 1 ms to excite COM motion, resulting in a decrease in fluorescence from Doppler shifts when heated.

Fig. 8 shows an example of interleaved tracking of the axial COM frequency and qubit frequency during a simulation of the Dicke model. For a given simulation, the dynamics are evolved for 100 different time steps from 0 to 3 ms, with 30 repeats at each time step and 5 passes over all time steps, giving a total of 15,000 measurements of the dynamics. Approximately every 150 measurements of the dynamics, the COM and qubit frequency were measured using ~ 30 repetitions of each side fringe and ~ 10 repetitions of the center frequency. From the statistical uncertainties of the measured populations the tracked frequencies are estimated to a precision of $\sim \pm 1$ and $\sim \pm 4$ Hz for the COM and qubit frequencies respectively. Drifts over the course of a scan would have resulted in errors of ~ 100 Hz for most simulations without active compensation.

Appendix B: Theoretical model

Here we describe our theoretical model, which captures relevant experimental details and noise sources. First, we account for the effects of spontaneous emission of the ions, which primarily affects our microwave qubit transition through its off-resonant coupling to the finite lifetime electronic states via the applied crossed optical beams used to engineer the spin-dependent ODF, see e.g. [103, 104]. For our spin states, this effectively manifests as two different types of scattering processes that we may account for via appropriate jump operators within a Lindblad master equation approach [103, 104]: an elastic Rayleigh scattering process, which can be accounted for by the collection of independent jump operators $\{\sqrt{\Gamma_z/4}\hat{\sigma}_{z,j}\}$, and an inelastic Raman scattering process, which can be accounted for by the collection of independent jump operators $\{\sqrt{\Gamma_{\uparrow\downarrow}}\hat{\sigma}_{-,j}\}$ and $\{\sqrt{\Gamma_{\uparrow\downarrow}}\hat{\sigma}_{+,j}\}$. The relevant branching ratios of these different processes may be calculated from the relevant ODF and atomic parameters [103, 104], and we take $\Gamma_{\uparrow\downarrow}/\Gamma_{\text{tot}} = 0.12$, $\Gamma_{\downarrow\uparrow}/\Gamma_{\text{tot}} = 0.08$, $\Gamma_z/\Gamma_{\text{tot}} = 0.80$, where $\Gamma_{\text{tot}} = \Gamma_z + \Gamma_{\uparrow\downarrow} + \Gamma_{\downarrow\uparrow} \sim 100 - 140 \text{ s}^{-1}$ describes the decay of the transverse magnetization arising from the ODF beams in a Ramsey-type experiment: $\langle \hat{S}_x(t) \rangle = \langle \hat{S}_x(0) \rangle e^{-\Gamma_{\text{tot}}t/2}$.

We also account for the role of low-frequency magnetic field fluctuations in the experiment. In principle, this can be modeled by including a global z -field, whose amplitude dynamically fluctuates with an appropriate power spectral density (PSD) matching that characterized in the experiment. Here, however, we opt for a simplified phenomenological model, where we split this noise into a quasi-static component, whose amplitude experiences shot-to-shot random variations described by a normal distribution $\mathcal{N}(0, \sigma_B^2)$, and a pure white-noise dynamical contribution, described by a jump operator $\sqrt{\Gamma_B}\hat{S}_z$ within a Lindblad master equation approach. The quasi-static/white-noise terms separately account for contributions to the magnetic field noise that fluctuate on timescales slow/fast compared to the relevant experimental timescale for each shot of the experiment. In order to choose the appropriate parameters for our model, we set Γ_B and σ_B to reproduce the expected Gaussian decay rates from a Ramsey-type experiment in the absence of the ODF beams. For an initial spin state $| (N/2)_x \rangle$, we fit the spin contrast decay as $2 \langle \hat{S}_x \rangle / N = e^{-(\gamma_{\text{exp}} t)^2/2}$, and find that using $\Gamma_B = 150 \text{ s}^{-1}$ and $\sigma_B = 2\pi \times 45 \text{ Hz}$ in our model well reproduces the observed fitted gaussian decay rates.

Finally, we account for the effects of previously studied quasi-static variations in the COM frequency [32], which we model as an effective shot-to-shot variation in the COM detuning, where we let $\delta \rightarrow \delta + \tilde{\delta}$ where $\tilde{\delta}$ is a random variable drawn from a normal distribution $\mathcal{N}(0, \sigma_{\delta}^2)$ for fixed $\sigma_{\delta} = 2\pi \times 40 \text{ Hz}$.

In all, our dynamical evolution is described by the Lindblad master equation

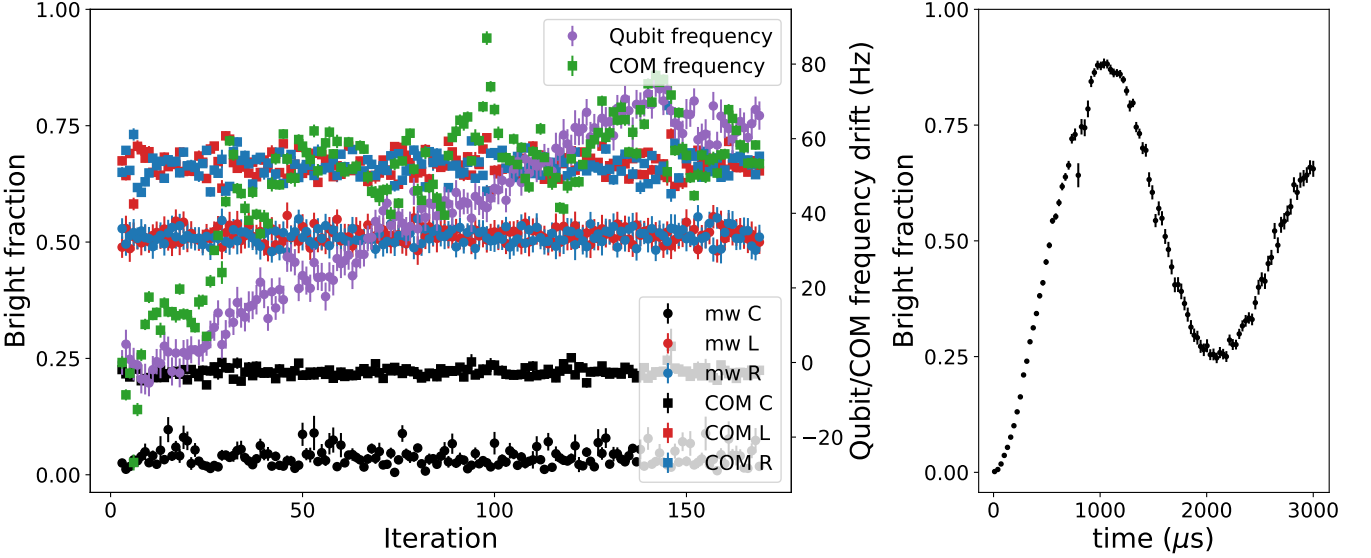


FIG. 8. Example Dicke model simulation with interleaved tracking. The right plot shows the simulated Dicke model dynamics with $\Omega/\delta = 0.125$ and $\Omega/\chi = 0.91$. Approximately every ~ 150 measurements a COM and qubit frequency tracker measurement was carried out as shown on the left plot. On the left vertical axis is the bright fraction corresponding to the left (red), right (blue), and center (black) measurements for the qubit (circles) and COM (squares) frequency trackers. The right vertical axis shows the tracked center microwave qubit (purple circles) and COM (green squares) frequencies, offset by their starting values of 124.022438607 GHz and 1.591254 MHz respectively. Estimated uncertainties suggest the center frequencies are tracked to $\sim \pm 1$ and $\sim \pm 4$ Hz for the COM and qubit frequencies respectively. Drifts of the center frequencies over the course of the scan suggest without active feedback errors of order 100 Hz would have occurred.

$$\frac{d}{dt}\hat{\rho}(t) = \frac{-i}{\hbar} [\hat{H}_{\text{tot}}, \hat{\rho}(t)] + \frac{\Gamma_z}{4} \sum_j \mathcal{D}[\hat{\sigma}_{z,j}]\hat{\rho}(t) + \Gamma_{\uparrow\downarrow} \sum_j \mathcal{D}[\hat{\sigma}_{-,j}]\hat{\rho}(t) + \Gamma_{\downarrow\uparrow} \sum_j \mathcal{D}[\hat{\sigma}_{+,j}]\hat{\rho}(t) + \Gamma_B \mathcal{D}[\hat{S}_z]\hat{\rho}(t) \quad (\text{B1})$$

for Lindblad superoperators $\mathcal{D}[\hat{O}]\hat{\rho} \equiv \hat{O}\hat{\rho}\hat{O}^\dagger - \{\hat{O}^\dagger\hat{O}, \hat{\rho}\}/2$ and anti-commutator $\{\cdot, \cdot\}$, and where the total Hamiltonian is defined by $\hat{H}_{\text{tot}} = \hat{H}_{\text{Dicke}} + \hat{H}_{\text{rand}}$ with

$$\hat{H}_{\text{rand}}/\hbar = -\tilde{\delta}\hat{a}^\dagger\hat{a} + B\hat{S}_z, \quad (\text{B2})$$

where $\tilde{\delta}$ and B are random variables drawn from the appropriate distributions described above. We then compute expectation values of observable operators \hat{O} via $O(t) \equiv \mathbb{E}[\langle \hat{O}(t) \rangle]$, where $\langle \hat{O}(t) \rangle = \text{Tr}[\hat{O}\hat{\rho}(t)]$ and $\mathbb{E}[\cdot]$ denotes expectations with respect to the distributions for $\tilde{\delta}$ and B .

For our initial state, as described in Fig. 1(a) of the main text, we let $\hat{\rho}(0) = \hat{\rho}_\nu \equiv \hat{\rho}_{\text{th}} \otimes |(-N/2)_\nu\rangle\langle(-N/2)_\nu|$, where $\nu = z, x$ depending on the relevant spin state we consider, and $\hat{\rho}_{\text{th}}$ is a thermal state of the phonons, given

in a Fock state basis via

$$\hat{\rho}_{\text{th}} \equiv \frac{1}{Z} \sum_{n=0}^{\infty} e^{-\beta\hbar\omega_Z n} |n\rangle\langle n|, \quad Z = \sum_{n=0}^{\infty} e^{-\beta\hbar\omega_Z n} \quad (\text{B3})$$

for inverse temperature $\beta \equiv 1/k_B T$, where k_B is the Boltzmann factor and T is the temperature. In terms of the initial thermal occupation $\bar{n} \equiv \text{Tr}[\hat{\rho}(0)\hat{a}^\dagger\hat{a}]$, we have $\beta\hbar\omega_Z = \ln(1 + 1/\bar{n})$.

We make two comments regarding this model. First, note that since

$$(\mathcal{D}[\hat{\sigma}_{-,j}] + \mathcal{D}[\hat{\sigma}_{+,j}])\hat{\rho}(t) = \frac{1}{2}(\mathcal{D}[\hat{\sigma}_{x,j}] + \mathcal{D}[\hat{\sigma}_{y,j}])\hat{\rho}(t), \quad (\text{B4})$$

then with $\Gamma_{\uparrow\downarrow} \geq \Gamma_{\downarrow\uparrow}$, we have

$$(\Gamma_{\uparrow\downarrow}\mathcal{D}[\hat{\sigma}_{-,j}] + \Gamma_{\downarrow\uparrow}\mathcal{D}[\hat{\sigma}_{+,j}])\hat{\rho}(t) = \frac{\Gamma_{\downarrow\uparrow}}{2}(\mathcal{D}[\hat{\sigma}_{x,j}] + \mathcal{D}[\hat{\sigma}_{y,j}])\hat{\rho}(t) + (\Gamma_{\uparrow\downarrow} - \Gamma_{\downarrow\uparrow})\mathcal{D}[\hat{\sigma}_{-,j}]\hat{\rho}(t). \quad (\text{B5})$$

We use this formulation in our semiclassical model, outlined in Appendix D.

Second, for the initial state $\hat{\rho}_z$, explored in Figs. 2, 3, the dynamics of $\mathbb{E}[\langle \hat{S}_z \rangle]$ are invariant with respect to the sign of δ . Likewise, for the initial state $\hat{\rho}_x$ utilized in Figs. 4 and 5, the dynamics of $\mathbb{E}[\langle \hat{S}_x \rangle]$ are also invariant with respect to inverting the sign of δ if we also invert the sign of Ω .

$$\begin{aligned} \frac{d}{dt} \tilde{\mathcal{S}}_z &= \Omega \tilde{\mathcal{S}}_y - (\Gamma_{\uparrow\downarrow} + \Gamma_{\downarrow\uparrow}) \tilde{\mathcal{S}}_z - \left(\frac{\Gamma_{\uparrow\downarrow} - \Gamma_{\downarrow\uparrow}}{2} \right), & \frac{d}{dt} \tilde{\mathcal{S}}_y &= -\Omega \tilde{\mathcal{S}}_x + 2g \tilde{\mathcal{S}}_x (\tilde{\alpha} + \tilde{\alpha}^*) + B \tilde{\mathcal{S}}_x - \left(\frac{\Gamma_z + \Gamma_{\uparrow\downarrow} + \Gamma_{\downarrow\uparrow} + \Gamma_B}{2} \right) \tilde{\mathcal{S}}_y \\ \frac{d}{dt} \tilde{\mathcal{S}}_x &= -2g \tilde{\mathcal{S}}_y (\tilde{\alpha} + \tilde{\alpha}^*) - B \tilde{\mathcal{S}}_y - \left(\frac{\Gamma_z + \Gamma_{\uparrow\downarrow} + \Gamma_{\downarrow\uparrow} + \Gamma_B}{2} \right) \tilde{\mathcal{S}}_x, & \frac{d}{dt} \tilde{\alpha} &= i(\delta + \tilde{\delta}) \tilde{\alpha} - 2ig \tilde{\mathcal{S}}_z, \end{aligned} \quad (C1)$$

for fixed $\tilde{\delta}$, B . At this level, the effects of collective and individual dephasing are indistinguishable from each other. The system size dependence also drops out from these equations in our normalization of the corresponding classical variables.

For the dynamics considered in the main text, $\langle \hat{a}(0) \rangle = \text{Tr}[\hat{\rho}_{\text{th}} \hat{a}] = 0$ and $\langle \hat{S}_\mu(0) \rangle = \langle (-N/2)_\nu | \hat{S}_\mu | (-N/2)_\nu \rangle = -N\delta_{\mu\nu}/2$ for the initial state $\hat{\rho}_\nu = \hat{\rho}_{\text{th}} \otimes |(-N/2)_\nu \rangle \langle (-N/2)_\nu|$, with $\nu = z$ for Fig. 1-3 or $\nu = x$ for Figs. 4 and 5. Thus, for our MF model of the dynamics, we evolve Eq. (C1) with initial conditions $\tilde{\alpha} = 0$ and $\tilde{\mathcal{S}}_\mu = -\delta_{\mu\nu}/2$. To account for quasi-static noise in the evolution, we average all observables over an ensemble of $n_{\text{traj}} = 10^3$ solutions—or trajectories—each computed for a different choice of $\tilde{\delta}$, B drawn from their respective distributions, so that our MF prediction for the spin dynamics is given by $\mathbb{E}[\langle \hat{S}_\mu \rangle] \rightarrow N \times \mathbb{E}[\tilde{\mathcal{S}}_\mu]$. Where relevant, we also have the MF prediction for the phonon dynamics $\mathbb{E}[\hat{\mathcal{X}}] \rightarrow \sqrt{2N} \times \mathbb{E}[\text{Re}\{\tilde{\alpha}\}]$ and $\mathbb{E}[\hat{\mathcal{P}}] \rightarrow \sqrt{2N} \times \mathbb{E}[\text{Im}\{\tilde{\alpha}\}]$ for $\hat{\mathcal{X}} = (\hat{a} + \hat{a}^\dagger)/\sqrt{2}$, $\hat{\mathcal{P}} = i(\hat{a}^\dagger - \hat{a})/\sqrt{2}$. We note that in Fig. 1, as well as for the “ideal” results shown in Fig. 2d, we take $\sigma_\delta, \sigma_B = 0$, as well as $\Gamma_z = \Gamma_{\uparrow\downarrow} = \Gamma_{\downarrow\uparrow} = \Gamma_B = 0$.

Appendix D: Semiclassical dynamics

For our semiclassical model, which accounts for beyond MF effects arising from both quantum and thermal fluctuations, we employ a discrete, dissipative version of the truncated Wigner approximation (TWA) [33, 69, 105, 106] that enables a treatment of both collective as well as individual dynamical noise sources in the spins. In essence, this approximation consists of evolving the MF equations of motion for \hat{H}_{tot} for n_{traj} random choices

Appendix C: Mean-field dynamics

Let us define classical, mean-field (MF) variables $\tilde{\mathcal{S}}_\mu$ and $\tilde{\alpha}$, representing the expectation values of $\langle \hat{S}_\mu \rangle / N$ and $\langle \hat{a} \rangle / \sqrt{N}$, respectively. Then, for evolution described by Eq. (B1), we have equations of motion within the MF approximation

of our initial conditions, and averaging relevant observables over the ensemble of resulting dynamical trajectories. This sampling reproduces the effect of both thermal and quantum fluctuations in our initial state, and can provide an accurate approximation of these fluctuations in the dynamics.

Similar to Appendix C, quasi-static noise may be accounted for by different choices of B and $\tilde{\delta}$ for each trajectory. We also supplement the MF evolution for our Hamiltonian with stochastic terms, which properly account for the effects of dynamical noise modeled by our jump operators in the master equation. While Hermitian jump operators—such as those corresponding to Γ_z and Γ_B —may be readily modeled by classical stochastic fields, spontaneous emission and absorption ($\Gamma_{\uparrow\downarrow}, \Gamma_{\downarrow\uparrow}$) corresponding to an amplitude damping channel require a more elaborate approach. We first rewrite the relevant Lindblad terms as in Eq. (B5), where balanced contributions to decay and absorption may be equivalently modeled as independent $\hat{\sigma}_{x,j}$ and $\hat{\sigma}_{y,j}$ channels that are exactly modeled within our approach (up to statistical errors, and errors arising from the MF treatment of the unitary evolution). For the residual unbalanced evolution, proportional to $\Gamma_{\uparrow\downarrow} - \Gamma_{\downarrow\uparrow}$, we opt for an approximate approach outlined in Ref. [106], which remains valid in the limit of small noise. In any case, as the main dynamical noise contributions arise from individual dephasing ($\Gamma_z/\Gamma_{\text{tot}} = 0.80$), and the spontaneous decay/absorption rates are relatively balanced ($\Gamma_{\uparrow\downarrow}/\Gamma_{\text{tot}} = 0.12$, $\Gamma_{\downarrow\uparrow}/\Gamma_{\text{tot}} = 0.08$), we don’t expect effects from this unbalanced decay, much less errors from our approximate treatment, to play any consequential role in the evolution.

Let $\mathcal{S}_{\mu,j}$ represent the expectation value of $\langle \hat{\sigma}_{\mu,j} \rangle / 2$, and α represent the expectation value of $\langle \hat{a} \rangle$. Then, the relevant evolution equations for each trajectory are given by the Stratonovich stochastic differential equations

$$d\mathcal{S}_{z,j} = \left[\Omega \mathcal{S}_{y,j} - \frac{3}{2} (\Gamma_{\uparrow\downarrow} - \Gamma_{\downarrow\uparrow}) (\mathcal{S}_{z,j} + 1/2) \right] dt + \sqrt{2\Gamma_{\uparrow\downarrow}} (\mathcal{S}_{y,j} dW_{x,j}(t) - \mathcal{S}_{x,j} dW_{y,j}(t)) + \sqrt{\Gamma_{\uparrow\downarrow} - \Gamma_{\downarrow\uparrow}} (\mathcal{S}_{z,j} + 1/2) dW_{d,j}(t) \quad (D1)$$

$$d\mathcal{S}_{y,j} = \left[-\Omega \mathcal{S}_{x,j} + \frac{2g}{\sqrt{N}} \mathcal{S}_{x,j} (\alpha + \alpha^*) + B \mathcal{S}_{x,j} \right] dt - \sqrt{2\Gamma_{\downarrow\uparrow}} \mathcal{S}_{z,j} dW_{x,j}(t) + \sqrt{\Gamma_z} \mathcal{S}_{x,j} dW_{z,j}(t) + \sqrt{\Gamma_B} \mathcal{S}_{x,j} dW_B(t) + \sqrt{\Gamma_{\uparrow\downarrow} - \Gamma_{\downarrow\uparrow}} \mathcal{S}_{x,j} dW_{d,j}(t) \quad (D2)$$

$$d\mathcal{S}_{x,j} = \left[-\frac{2g}{\sqrt{N}} \mathcal{S}_{y,j} (\alpha + \alpha^*) - B \mathcal{S}_{y,j} \right] dt + \sqrt{2\Gamma_{\uparrow\downarrow}} \mathcal{S}_{z,j} dW_{y,j}(t) - \sqrt{\Gamma_z} \mathcal{S}_{y,j} dW_{z,j}(t) - \sqrt{\Gamma_B} \mathcal{S}_{y,j} dW_B(t) - \sqrt{\Gamma_{\uparrow\downarrow} - \Gamma_{\downarrow\uparrow}} \mathcal{S}_{y,j} dW_{d,j}(t) \quad (D3)$$

$$d\alpha = i \left[(\delta + \tilde{\delta}) \alpha - \frac{2g}{\sqrt{N}} \sum_j \mathcal{S}_{z,j} \right] dt. \quad (D4)$$

Here, $dW_{\mu,j}(t)$ are independent, real Wiener increments for $\mu = x, y, z$ and $j = 1, \dots, N$, describing individual dephasing along each axis; $dW_B(t)$ is a real Wiener increment describing global dephasing; and $dW_{d,j}(t)$ for $j = 1, \dots, N$ are real, independent Wiener increments corresponding to residual imbalanced decay/absorption for each qubit. These stochastic Wiener increments are chosen independently for each trajectory and timestep such that $\mathbb{E}[dW(t)dW(t')] = dt\delta_{t,t'}$, where t, t' denote timestep labels and $\mathbb{E}[\cdot]$ denotes averaging over all trajectories (and distinct Wiener increments are always chosen independently). For our semi-implicit solver, we utilize a typical timestep $dt = 2 \mu\text{s}$.

For initializing each trajectory, we set $\mathcal{S}_{\mu,j} = \pm 1/2$ with equal probability, independently for each $\mu \neq \nu$ and j , and set $\mathcal{S}_{\nu,j} = -1/2$ for initial state $\hat{\rho}_\nu$. Meanwhile, we choose $\text{Re}\{\alpha\}$ and $\text{Im}\{\alpha\}$ independently from a distribution $\mathcal{N}(0, \bar{n}/2 + 1/4)$; even as $\bar{n} \rightarrow 0$, there is residual noise reflecting vacuum fluctuations of the phonon mode. We thus have that $\mathbb{E}[\alpha] = 0$, $\mathbb{E}[\alpha^* \alpha] = \bar{n} + 1/2$, where the latter quantity corresponds to the Weyl-ordered observable $\langle (\hat{a}^\dagger \hat{a} + \hat{a} \hat{a}^\dagger)/2 \rangle = \langle \hat{a}^\dagger \hat{a} \rangle + 1/2$. For the calculation of observables within this semiclassical approximation, we have the correspondence $\mathbb{E}[\langle \hat{S}_\mu \rangle] \rightarrow \sum_j \mathbb{E}[\mathcal{S}_{\mu,j}]$, $\mathbb{E}[\langle \hat{\mathcal{X}} \rangle] \rightarrow \sqrt{2} \times \mathbb{E}[\text{Re}\{\alpha\}]$, and $\mathbb{E}[\langle \hat{\mathcal{P}} \rangle] \rightarrow \sqrt{2} \times \mathbb{E}[\text{Im}\{\alpha\}]$. We can also obtain estimates for Weyl-ordered correlators of different observables, e.g. via the correspondence $\mathbb{E}[\langle \hat{S}_\mu \hat{S}_\nu + \hat{S}_\nu \hat{S}_\mu \rangle/2] \rightarrow \sum_{j,j'} \mathbb{E}[\mathcal{S}_{\mu,j} \mathcal{S}_{\nu,j'}]$ and $\mathbb{E}[\langle \hat{a}^\dagger \hat{a} + \hat{a} \hat{a}^\dagger \rangle/2] \rightarrow \mathbb{E}[\alpha^* \alpha]$, and with analogous equations for mixed spin-phonon observables and correlators. Here, \mathbb{E} denotes averaging over all random trajectories, which incorporates averaging over all initial conditions and stochastic noise sources for our semiclassical model, as well as quasi-static noise terms in the Hamiltonian for both the semiclassical model and the full evolution.

In Fig. 9, 10, we utilize this semiclassical model to examine the effect of different noise sources in the evolution. We select parameters relevant to Figs. 3-5 in the

main text, for which we have closely examined the role of thermal noise. We note that for both sets of initial conditions, the main deviations of our results from the unitary dynamics are accounted for by magnetic field noise (Fig. 9, yellow dotted line). Light scattering from the ODF beams (Fig. 9, orange dotted line) and initial thermal occupation of the phonons (Fig. 10, green dotted line) play a noticeable but less prominent role, particularly for the x polarized initial state when operating in the near-integrable regime. In all cases, COM noise (Fig. 10, pink dotted line) plays virtually no role in the observed spin dynamics, so far as we are independently considering the effects of different noise sources within our model. Magnetic field noise can be mitigated in future experiments by floating the optical table [95, 97], or by performing a spin-echo sequence compatible with the Dicke Hamiltonian. Furthermore, increased ODF power and stronger microwave drives can speed up the dynamics relative to the magnetic field decoherence rates.

In Fig. 4c of the main text, we closely examined the effects of thermal noise on the x polarized initial state, suggesting that the observed dynamics are largely driven by quantum fluctuations in the initial state. However, we also note from Fig. 11 that for our z polarized initial state in the chaotic (middle panel, denoted by the green star) and untrapped phases (left panel, denoted by the green circle), the ideal solutions, which neglect the effects of thermal noise appear to differ considerably from the MF solution shown in the main text (see Fig. 3), suggesting that even here, quantum fluctuations play a dominant role in the observed damping compared to the classical solution.

For the analysis in Fig. 4c, we showed results for a classical model where we take into account the effects of varying levels of thermal noise in the phonons. This model is essentially the semiclassical model outlined here, except that we initialize $\mathcal{S}_{\mu,j}$ at its MF values for each trajectory (i.e. $\mathcal{S} = (-1/2, 0, 0)$), and draw $\text{Re}\{\alpha\}$ and $\text{Im}\{\alpha\}$ independently from a distribution $\mathcal{N}(0, \bar{n}/2)$. Thus, for

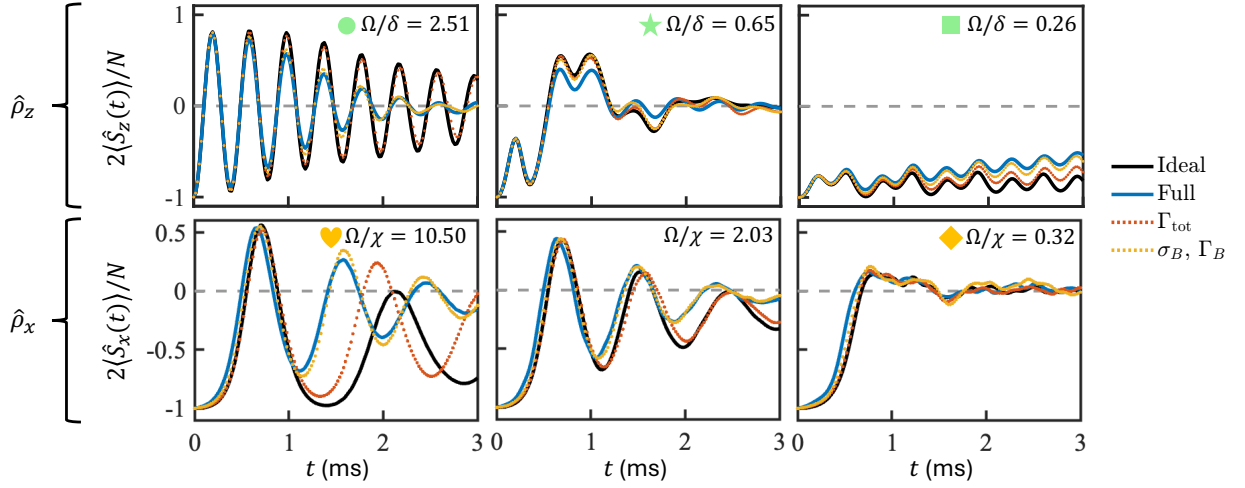


FIG. 9. Characterization of noise sources on spin degree of freedom in semiclassical model. (Top) We re-plot the results for the EIT cooled initial conditions from Fig. 3, showing the results of our semiclassical model when different noise sources are included. We show our full results (blue solid), as well as the ideal semiclassical model (only including effects of \hat{H}_{Dicke} , with an initial vacuum state for the phonons; black solid). Other dotted lines show results of ideal evolution in addition to either light scattering from the ODF beams characterized by the total rate Γ_{tot} (orange dotted), or quasi-static collective magnetic field noise, with field amplitude B chosen from a normal distribution $\mathcal{N}(0, \sigma_B^2)$ and dynamical collective magnetic field noise (with a white-noise spectrum) with decay rate Γ_B (yellow dotted). (Bottom) We also show analogous results corresponding to the results from Figs. 4 in the main text.

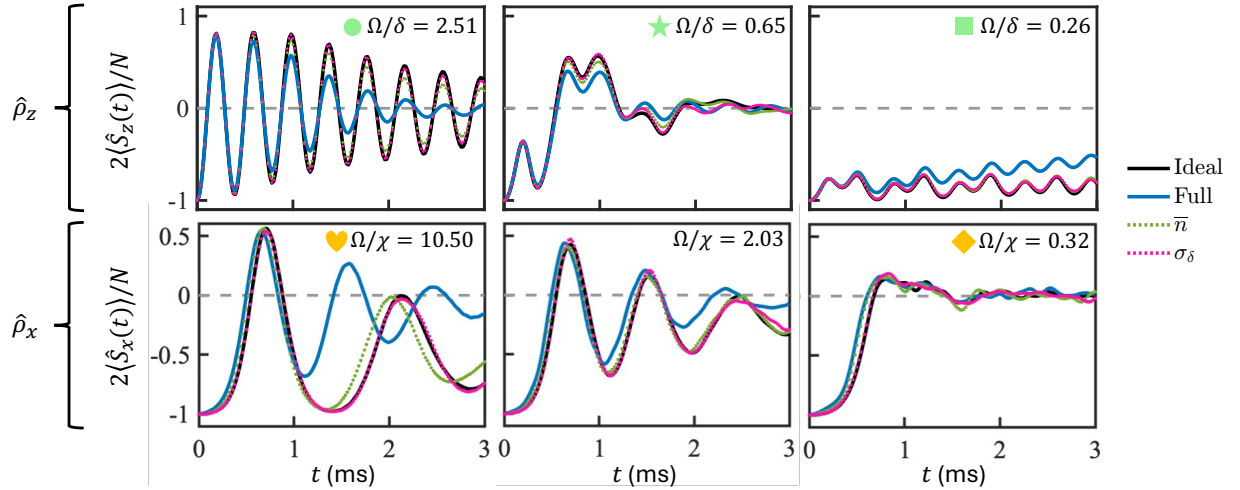


FIG. 10. Characterization of noise sources on phonon degree of freedom in semiclassical model. Analogous plot to Fig. 9, where we instead show results of ideal evolution in addition to either initial thermal noise in the phonons, with initial occupancy $n_0 \sim 0.5$ (green dotted), or quasi-static COM noise, with $\delta \rightarrow \delta + \tilde{\delta}$ for $\tilde{\delta}$ chosen from a normal distribution $\mathcal{N}(0, \sigma_\delta^2)$ (pink dotted). Full results with all noise sources (blue solid) as well as the ideal semiclassical model (black solid) are also plotted.

$\bar{n} \rightarrow 0$, we recover the MF model up to our stochastic treatment of the individual decoherence processes. In this way, we ensure the *only* differences between the TWA solution and our classical, thermal solutions are the absence of projection noise in the spins and the absence of vacuum noise in the phonons.

Appendix E: Computing phase space plots

For the dynamical phase space plots in Fig. 3, we plot the trajectory of the mean spin dynamics in terms of $\langle \hat{S}_z(t) \rangle$ and $\langle \hat{S}_y(t) \rangle$. From the equations of motion for unitary evolution under \hat{H}_{Dicke} , we have that $d \langle \hat{S}_z \rangle / dt = \Omega \langle \hat{S}_y \rangle$, so that this forms a canonical phase space for the z -magnetization. It is therefore possible, in principle, to extract both the z and y collective spin components from

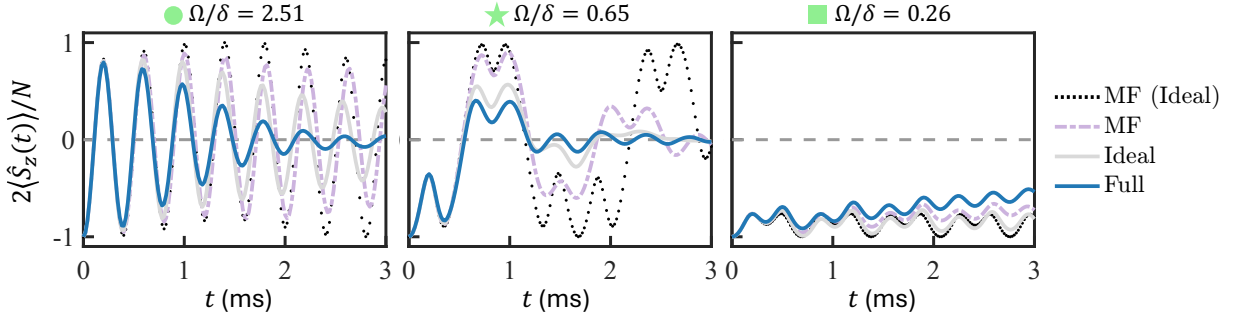


FIG. 11. Comparison of “chaotic cut” with and without technical noise sources. We re-plot the results for the EIT cooled initial conditions from Fig. 3, showing the results of our semiclassical (blue solid) and MF (lavender dashed-dot) models when all technical noise sources are included. We also show the corresponding ideal semiclassical (gray solid) and MF dynamics (black dotted).

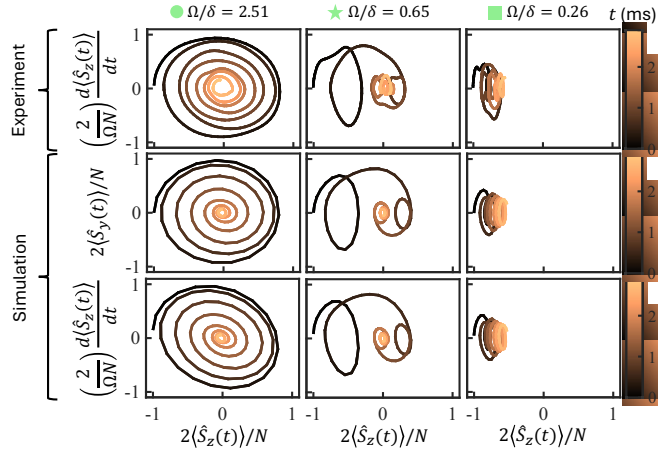


FIG. 12. Comparison of phase space plots. (Top) We plot the phase space plots from Fig. 3, computed from the experimental data, where the y-axis is obtained from smoothing of the experimental $\langle \hat{S}_z(t) \rangle$ and subsequently taking the numerical derivative. (Middle) We compare to the corresponding semiclassical model, incorporating technical noise sources, where the y-axis is instead obtained directly from simulation results for $\langle \hat{S}_y(t) \rangle$. (Bottom) We also compare to the semiclassical model, where the y-axis is instead computed from the numerical derivative for $\langle \hat{S}_z(t) \rangle$; while expected to be exact for ideal unitary evolution under \hat{H}_{Dicke} , up to errors arising from the finite timestep and statistical error from the number of trajectories, the presence of light scattering from the ODF beams invalidates any direct correspondence. Nonetheless, we observe fair agreement with our simulations to validate our approach.

the dynamics of $\langle \hat{S}_z(t) \rangle$ alone.

Before computing the derivative in time, we first apply a smoothing process to the data for $\langle \hat{S}_z(t) \rangle$, utilizing MATLAB’s smoothing spline with a smoothing parameter of $p = 0.98$, and utilizing the reciprocal variance of each timeseries point as a weighting function. In order to avoid issues arising from the smoothing process at the endpoints of the timeseries, we first mirror the data about $t = 0$ before smoothing, so that we have an effec-

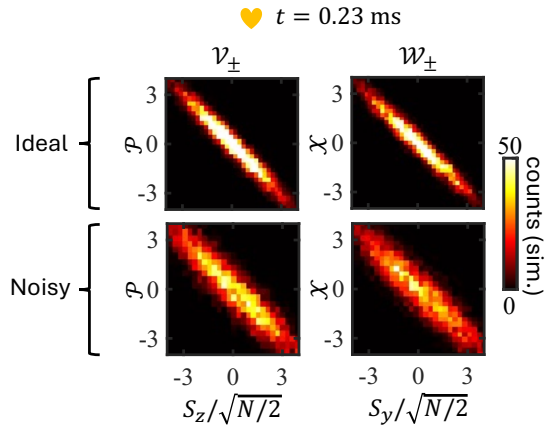


FIG. 13. Comparison of joint histograms for the squeezed/anti-squeezed mixed quadratures. (Top) We plot the histograms for the \mathcal{V}_\pm (left) and \mathcal{W}_\pm (right) quadratures obtained from ideal semiclassical evolution under \hat{H}_{Dicke} , analogous to the result from Fig. 5e,f computed in the presence of relevant technical noise sources, reiterated on the bottom for comparison.

tive timeseries for $t \in [-3.0, 3.0]$ ms — this effectively enforces a local extremum at $t = 0$, so that the resulting derivative vanishes at this point, resulting in the expected condition $d \langle \hat{S}_z(t) \rangle / dt|_{t=0} \propto \langle \hat{S}_y(0) \rangle = 0$. For the opposite endpoint at the maximum evolution time, we simply truncate the displayed data to a maximum time of $t = 2.9$ ms.

We find that this process is suitable for removing local fluctuations of the time derivative owing to small variations in the mean value of neighboring time points, while not significantly altering trends in the global dataset. In Fig. 12, we directly compare our phase space plots using the smoothed experimental data to direct theoretical calculations of the y -magnetization, via our semiclassical model, finding that our smoothing process and numerical derivative provide a good representations for the dynamics of $\langle \hat{S}_y(t) \rangle$.

Appendix F: Holstein-Primakoff approximation

For evolution under \hat{H}_{Dicke} in the resonant case with $\Omega = \delta$, let us define rotated spin ladder operators, $\hat{S}_{\pm}^{(x)} \equiv \hat{S}_y \pm i\hat{S}_z$, such that $\hat{S}_z = -i(\hat{S}_+^{(x)} - \hat{S}_-^{(x)})/2$, $\hat{S}_y = (\hat{S}_+^{(x)} + \hat{S}_-^{(x)})/2$, and which act on eigenstates of \hat{S}_x as $\hat{S}_{\pm}^{\text{rot}} |(m)_x\rangle \propto |(m \pm 1)_x\rangle$. Thus, we may write

$$\hat{H}_{\text{Dicke}}/\hbar = -\delta\hat{a}^\dagger\hat{a} + \delta\hat{S}_x + \frac{-ig}{\sqrt{N}} (\hat{a} + \hat{a}^\dagger) (\hat{S}_+^{(x)} - \hat{S}_-^{(x)}). \quad (\text{F1})$$

In the rotating frame defined by $\hat{H}_0/\hbar = -\delta\hat{a}^\dagger\hat{a} + \delta\hat{S}_x$, we obtain the Hamiltonian $\hat{H}^{\text{rot}} = \hat{H}_{\text{pair}}^{\text{rot}} + \hat{H}_{\text{osc}}^{\text{rot}}$ where

$$\hat{H}_{\text{pair}}^{\text{rot}} \equiv \hbar \frac{-ig}{\sqrt{N}} (\hat{a}^\dagger \hat{S}_+^{(x)} - \hat{a} \hat{S}_-^{(x)}), \quad \hat{H}_{\text{osc}}^{\text{rot}} \equiv \hbar \frac{-ig}{\sqrt{N}} (\hat{a} \hat{S}_+^{(x)} e^{2i\delta t} - \hat{a}^\dagger \hat{S}_-^{(x)} e^{-2i\delta t}). \quad (\text{F2})$$

As $\delta \rightarrow \infty$, we may neglect the effects of $\hat{H}_{\text{osc}}^{\text{rot}}$ in the rotating wave approximation, whose terms rapidly oscillate, averaging to 0. For the remaining $\hat{H}_{\text{pair}}^{\text{rot}}$, we can then employ a Holstein-Primakoff (HP) approximation, valid for states with $(m)_x \sim -N/2$, where let $\hat{S}_{+,\text{rot}} \approx \sqrt{N}\hat{b}^\dagger$, $\hat{S}_{-,\text{rot}} \approx \sqrt{N}\hat{b}$ for bosonic creation/annihilation operators $\hat{b}^\dagger\hat{b}$ representing the collective spin mode. Then,

$$\hat{H}_{\text{pair}}^{\text{rot}} \approx -i\hbar g (\hat{a}^\dagger \hat{b}^\dagger - \hat{a} \hat{b}). \quad (\text{F3})$$

Now, let us define the mixed quadrature operators $\hat{c}_{\pm} = (\hat{a} \pm i\hat{b})/\sqrt{2}$, so that with $\hat{\mathcal{X}}_{\pm} = (\hat{c}_{\pm} + \hat{c}_{\pm}^\dagger)/\sqrt{2}$ and $\hat{\mathcal{P}}_{\pm} = i(\hat{c}_{\pm}^\dagger - \hat{c}_{\pm})/\sqrt{2}$ we have

$$\hat{H}_{\text{pair}}^{\text{rot}} \approx \frac{-\hbar g}{2} (\hat{\mathcal{P}}_+^2 - \hat{\mathcal{X}}_+^2 - \hat{\mathcal{P}}_-^2 + \hat{\mathcal{X}}_-^2). \quad (\text{F4})$$

The \hat{c}_{\pm} modes thus correspond to two independent, inverted mass oscillators. For the initial state $\hat{\rho}_x$ with $\bar{n} = 0$, this corresponds to the joint vacuum state $|0\rangle_a \otimes |0\rangle_b$ for our bosonic degrees of freedom within the Holstein-Primakoff approximation. Evolved under the dynamics of Eq. (F4), this results in the squeezing of the mixed quadratures $\hat{\mathcal{P}}_{\pm} \pm \hat{\mathcal{X}}_{\pm}$, as well as the anti-squeezing of the canonically conjugate quadratures $\hat{\mathcal{P}}_{\pm} \mp \hat{\mathcal{X}}_{\pm}$. Thus, any

linear combination of these two squeezed/anti-squeezed quadratures will likewise be squeezed/anti-squeezed.

In terms of our original phonon and collective spin operators, the simplest such combinations are given by $\hat{\mathcal{V}}_{\pm} = [(\hat{\mathcal{P}}_{-} \mp \hat{\mathcal{X}}_{-}) + (\hat{\mathcal{P}}_{+} \pm \hat{\mathcal{X}}_{+})]/\sqrt{2} \approx \hat{\mathcal{P}} \pm \hat{S}_z/\sqrt{N/2}$ and $\hat{\mathcal{W}}_{\pm} = [(\hat{\mathcal{P}}_{-} \pm \hat{\mathcal{X}}_{-}) - (\hat{\mathcal{P}}_{+} \mp \hat{\mathcal{X}}_{+})]/\sqrt{2} \approx \hat{\mathcal{X}} \pm \hat{S}_y/\sqrt{N/2}$, where the variances $\text{Var}(\hat{\mathcal{V}}_{+})$ and $\text{Var}(\hat{\mathcal{W}}_{+})$ will be dynamically reduced exponentially below their vacuum values of 1.

In Fig. 13, we show joint histograms for the various joint spin-phonon quadratures, analogous to Fig. 5e,f of the main text. These are computed in our semiclassical model outlined in Appendix D by plotting the relevant histogram for our ensemble of dynamical trajectories. On the top, we show quadrature distributions without noise, for which the evolution at short times is relatively similar, up to correlation/anti-correlation of the relevant quadratures. The presence of technical noise generally leads to a reduction in the overall amount of squeezing for each quadrature. However, even in ideal case, we find that the $\hat{\mathcal{V}}_{+}$ quadrature (left) remains more squeezed than the $\hat{\mathcal{W}}_{+}$ quadrature (right)—an asymmetry arising from the curvature of the Bloch sphere and breakdown of the HP approximation.

- [1] R. H. Dicke, *Physical Review* **93**, 99 (1954).
- [2] K. Hepp and E. H. Lieb, *Annals of Physics* **76**, 360 (1973).
- [3] R. J. Lewis-Swan, J. C. Z. Castro, D. Barberena, and A. M. Rey, *Physical Review Letters* **132**, 163601 (2024).
- [4] R. J. Lewis-Swan, A. Safavi-Naini, J. J. Bollinger, and A. M. Rey, *Nature Communications* **10**, 1581 (2019).
- [5] C. Emary and T. Brandes, *Physical Review E* **67**, 066203 (2003).
- [6] C. Emary and T. Brandes, *Physical Review Letters* **90**, 044101 (2003).
- [7] T. Brandes, *Physical Review E* **88**, 032133 (2013).
- [8] J. Klinder, H. Keßler, M. Wolke, L. Mathey, and A. Hemmerich, *Proceedings of the National Academy of Sciences* **112**, 3290 (2015).
- [9] A. T. Black, H. W. Chan, and V. Vuletić, *Physical Review Letters* **91**, 203001 (2003).
- [10] P. Domokos and H. Ritsch, *Journal of the Optical Society of America B* **20**, 2460 (2003).

ety of America B **20**, 1098 (2003).

[11] K. Baumann, C. Guerlin, F. Brennecke, and T. Esslinger, *Nature* **464**, 1301 (2010).

[12] D. Nagy, G. Kónya, G. Szirmai, and P. Domokos, *Physical Review Letters* **104**, 130401 (2010).

[13] F. Brennecke, R. Mottl, K. Baumann, R. Landig, T. Donner, and T. Esslinger, *Proceedings of the National Academy of Sciences* **110**, 11763 (2013).

[14] J. Léonard, A. Morales, P. Zupancic, T. Esslinger, and T. Donner, *Nature* **543**, 87 (2017).

[15] A. J. Kollár, A. T. Papageorge, V. D. Vaidya, Y. Guo, J. Keeling, and B. L. Lev, *Nature Communications* **8**, 1 (2017).

[16] M. Landini, N. Dogra, K. Kroeger, L. Hruba, T. Donner, and T. Esslinger, *Physical Review Letters* **120**, 223602 (2018).

[17] A. Morales, D. Dreon, X. Li, A. Baumgärtner, P. Zupancic, T. Donner, and T. Esslinger, *Physical Review A* **100**, 013816 (2019).

[18] Z. Yan, J. Ho, Y.-H. Lu, S. J. Masson, A. Asenjo-Garcia, and D. M. Stamper-Kurn, *Physical Review Letters* **131**, 253603 (2023).

[19] F. Yoshihara, T. Fuse, S. Ashhab, K. Kakuyanagi, S. Saito, and K. Semba, *Nature Physics* **13**, 44 (2017).

[20] P. Forn-Díaz, L. Lamata, E. Rico, J. Kono, and E. Solano, *Reviews of Modern Physics* **91**, 025005 (2019).

[21] Y. Todorov, A. M. Andrews, R. Colombelli, S. De Liberato, C. Ciuti, P. Klang, G. Strasser, and C. Sirtori, *Physical Review Letters* **105**, 196402 (2010).

[22] J. Marino, M. Eckstein, M. S. Foster, and A. M. Rey, *Reports on Progress in Physics* **85**, 116001 (2022).

[23] A. Smerzi, S. Fantoni, S. Giovanazzi, and S. R. Shenoy, *Physical Review Letters* **79**, 4950 (1997).

[24] M. Albiez, R. Gati, J. Fölling, S. Hunsmann, M. Cristiani, and M. K. Oberthaler, *Physical Review Letters* **95**, 010402 (2005).

[25] M. Abbarchi, A. Amo, V. G. Sala, D. D. Solnyshkov, H. Flayac, L. Ferrier, I. Sagnes, E. Galopin, A. Lemaître, G. Malpuech, and J. Bloch, *Nature Physics* **9**, 275 (2013).

[26] A. Reinhard, J.-F. Riou, L. A. Zundel, D. S. Weiss, S. Li, A. M. Rey, and R. Hipolito, *Physical Review Letters* **110**, 033001 (2013).

[27] J. Zhang, G. Pagano, P. W. Hess, A. Kyprianidis, P. Becker, H. Kaplan, A. V. Gorshkov, Z.-X. Gong, and C. Monroe, *Nature* **551**, 601 (2017).

[28] V. Borish, O. Marković, J. A. Hines, S. V. Rajagopal, and M. Schleier-Smith, *Physical Review Letters* **124**, 063601 (2020).

[29] J. A. Muniz, D. Barberena, R. J. Lewis-Swan, D. J. Young, J. R. K. Cline, A. M. Rey, and J. K. Thompson, *Nature* **580**, 602 (2020).

[30] Z. Li, S. Colombo, C. Shu, G. Velez, S. Pilatowsky-Cameo, R. Schmied, S. Choi, M. Lukin, E. Pedrozo-Peñaflor, and V. Vuletić, *Science* **380**, 1381 (2023).

[31] R. J. Lewis-Swan, S. R. Muleady, D. Barberena, J. J. Bollinger, and A. M. Rey, *Physical Review Research* **3**, L022020 (2021).

[32] K. A. Gilmore, M. Affolter, R. J. Lewis-Swan, D. Barberena, E. Jordan, A. M. Rey, and J. J. Bollinger, *Science* **373**, 673 (2021).

[33] D. Barberena, S. R. Muleady, J. J. Bollinger, R. J. Lewis-Swan, and A. M. Rey, *Quantum Science and Technology* **9**, 025013 (2024).

[34] P. Hayden and J. Preskill, *Journal of High Energy Physics* **2007**, 120 (2007).

[35] Y. Sekino and L. Susskind, *Journal of High Energy Physics* **2008**, 065 (2008).

[36] B. Yoshida and A. Kitaev, “Efficient decoding for the Hayden-Preskill protocol,” (2017), arXiv:1710.03363 [hep-th].

[37] B. Yoshida and N. Y. Yao, *Physical Review X* **9**, 011006 (2019).

[38] K. A. Landsman, C. Figgatt, T. Schuster, N. M. Linke, B. Yoshida, N. Y. Yao, and C. Monroe, *Nature* **567**, 61 (2019).

[39] M. S. Blok, V. V. Ramasesh, T. Schuster, K. O’Brien, J. M. Kreikebaum, D. Dahmen, A. Morvan, B. Yoshida, N. Y. Yao, and I. Siddiqi, *Physical Review X* **11**, 021010 (2021).

[40] Y. Cheng, C. Liu, J. Guo, Y. Chen, P. Zhang, and H. Zhai, *Physical Review Research* **2**, 043024 (2020).

[41] J.-M. Bae, S. Kang, D.-h. Yeom, and H. Zoe, *Journal of the Korean Physical Society* **75**, 941 (2019).

[42] J. Ho, Y.-H. Lu, T. Xiang, C. C. Rusconi, S. J. Masson, A. Asenjo-Garcia, Z. Yan, and D. M. Stamper-Kurn, *Nature Physics* **21**, 1071 (2025).

[43] A. Safavi-Naini, R. J. Lewis-Swan, J. G. Bohnet, M. Gärttner, K. A. Gilmore, J. E. Jordan, J. Cohn, J. K. Freericks, A. M. Rey, and J. J. Bollinger, *Physical Review Letters* **121**, 040503 (2018).

[44] I. Aedo and L. Lamata, *Physical Review A* **97**, 042317 (2018), arXiv:1802.01853 [quant-ph].

[45] R. T. Sutherland, *Physical Review A* **100**, 061405 (2019).

[46] J. G. Bohnet, B. C. Sawyer, J. W. Britton, M. L. Wall, A. M. Rey, M. Foss-Feig, and J. J. Bollinger, *Science* **352**, 1297 (2016), 27284189.

[47] J. J. Bollinger, J. W. Britton, and B. C. Sawyer, in *NON-NEUTRAL PLASMA PHYSICS VIII: 10th International Workshop on Non-Neutral Plasmas* (Greifswald, Germany, 2013) pp. 200–209.

[48] B. C. Sawyer, J. W. Britton, and J. J. Bollinger, *Physical Review A* **89**, 033408 (2014).

[49] K. A. Gilmore, J. G. Bohnet, B. C. Sawyer, J. W. Britton, and J. J. Bollinger, *Physical Review Letters* **118**, 263602 (2017).

[50] M. Affolter, K. A. Gilmore, J. E. Jordan, and J. J. Bollinger, *Physical Review A* **102**, 052609 (2020).

[51] J. W. Britton, B. C. Sawyer, A. C. Keith, C.-C. J. Wang, J. K. Freericks, H. Uys, M. J. Biercuk, and J. J. Bollinger, *Nature* **484**, 489 (2012).

[52] E. Jordan, K. A. Gilmore, A. Shankar, A. Safavi-Naini, J. G. Bohnet, M. J. Holland, and J. J. Bollinger, *Physical Review Letters* **122**, 053603 (2019).

[53] “See Supplemental Material at [URL will be inserted by publisher].”,”.

[54] P. Kirton, M. M. Roses, J. Keeling, and E. G. Dalla Torre, *Advanced Quantum Technologies* **2**, 1800043 (2019).

[55] M. Eckstein, M. Kollar, and P. Werner, *Physical Review Letters* **103**, 056403 (2009).

[56] M. Schiró and M. Fabrizio, *Physical Review Letters* **105**, 076401 (2010).

[57] B. Sciolla and G. Birolì, *Physical Review Letters* **105**, 220401 (2010).

[58] A. Gambassi and P. Calabrese, *Europhysics Letters* **95**,

66007 (2011).

[59] P. Smacchia, M. Knap, E. Demler, and A. Silva, *Physical Review B* **91**, 205136 (2015).

[60] H. J. Lipkin, N. Meshkov, and A. J. Glick, *Nuclear Physics* **62**, 188 (1965).

[61] P. Ribeiro, J. Vidal, and R. Mosseri, *Physical Review Letters* **99**, 050402 (2007).

[62] A. Lerose, B. Žunković, J. Marino, A. Gambassi, and A. Silva, *Physical Review B* **99**, 045128 (2019).

[63] V. Borish, O. Marković, J. A. Hines, S. V. Rajagopal, and M. Schleier-Smith, *Phys. Rev. Lett.* **124**, 063601 (2020).

[64] M. L. Wall, A. Safavi-Naini, and A. M. Rey, *Physical Review A* **95**, 013602 (2017).

[65] A. Lerose, J. Marino, B. Žunković, A. Gambassi, and A. Silva, *Physical Review Letters* **120**, 130603 (2018).

[66] A. Altland and F. Haake, *New Journal of Physics* **14**, 073011 (2012).

[67] J. Chávez-Carlos, M. A. Bastarrachea-Magnani, S. Lerma-Hernández, and J. G. Hirsch, *Physical Review E* **94**, 022209 (2016).

[68] S. Strogatz, *Nonlinear Dynamics and Chaos: With Applications to Physics, Biology, Chemistry, and Engineering*, Studies in Nonlinearity (Avalon Publishing, 2014).

[69] J. Schachenmayer, A. Pikovski, and A. M. Rey, *Physical Review X* **5**, 1 (2015).

[70] T. Holstein and H. Primakoff, *Physical Review* **58**, 1098 (1940).

[71] C. Gross, H. Strobel, E. Nicklas, T. Zibold, N. Bar-Gill, G. Kurizki, and M. K. Oberthaler, *Nature* **480**, 219 (2011).

[72] B. Lücke, M. Scherer, J. Kruse, L. Pezzé, F. Deuretzbacher, P. Hyllus, O. Topic, J. Peise, W. Ertmer, J. Arlt, L. Santos, A. Smerzi, and C. Klempert, *Science* **334**, 773 (2011).

[73] E. M. Bookjans, C. D. Hamley, and M. S. Chapman, *Physical Review Letters* **107**, 210406 (2011).

[74] A. T. Black, E. Gomez, L. D. Turner, S. Jung, and P. D. Lett, *Physical Review Letters* **99**, 070403 (2007).

[75] L. Zhao, J. Jiang, T. Tang, M. Webb, and Y. Liu, *Physical Review A* **89**, 023608 (2014).

[76] A. Qu, B. Evrard, J. Dalibard, and F. Gerbier, *Physical Review Letters* **125**, 033401 (2020).

[77] K. Kim, J. Hur, S. Huh, S. Choi, and J.-y. Choi, *Physical Review Letters* **127**, 043401 (2021).

[78] E. S. Polzik and J. Ye, *Physical Review A* **93**, 021404 (2016).

[79] G. Vasilakis, H. Shen, K. Jensen, M. Balabas, D. Salart, B. Chen, and E. S. Polzik, *Nature Physics* **11**, 389 (2015).

[80] J. Appel, P. J. Windpassinger, D. Oblak, U. B. Hoff, N. Kjærgaard, and E. S. Polzik, *Proceedings of the National Academy of Sciences* **106**, 10960 (2009).

[81] M. H. Schleier-Smith, I. D. Leroux, and V. Vuletić, *Physical Review Letters* **104**, 073604 (2010).

[82] J. G. Bohnet, K. C. Cox, M. A. Norcia, J. M. Weiner, Z. Chen, and J. K. Thompson, *Nature Photonics* **8**, 731 (2014).

[83] R. J. Sewell, M. Koschorreck, M. Napolitano, B. Dubost, N. Behbood, and M. W. Mitchell, *Physical Review Letters* **109**, 253605 (2012).

[84] H. Bao, J. Duan, S. Jin, X. Lu, P. Li, W. Qu, M. Wang, I. Novikova, E. E. Mikhailov, K.-F. Zhao, K. Mølmer, H. Shen, and Y. Xiao, *Nature* **581**, 159 (2020).

[85] D. F. Walls and G. J. Milburn, *Quantum Optics*, 2nd ed. (Springer, 2008).

[86] A. Rényi, *Berkeley Symposium on Mathematical Statistics and Probability* **4**, 547 (1961).

[87] K. Gietka, *Physical Review A* **110**, 063703 (2024).

[88] M. D. Reid, P. D. Drummond, W. P. Bowen, E. G. Cavalcanti, P. K. Lam, H. A. Bachor, U. L. Andersen, and G. Leuchs, *Reviews of Modern Physics* **81**, 1727 (2009).

[89] R. Uola, A. C. S. Costa, H. C. Nguyen, and O. Gühne, *Reviews of Modern Physics* **92**, 015001 (2020).

[90] Y. Takahashi and H. Umezawa, *Collective phenomena* **2**, 55 (1975).

[91] W. Israel, *Physics Letters A* **57**, 107 (1976).

[92] J. Maldacena, *Journal of High Energy Physics* **2003**, 021 (2003).

[93] J. Maldacena, D. Stanford, and Z. Yang, *Fortschritte der Physik* **65**, 1700034 (2017).

[94] B. B. Bullock, *Improved quantum control of two-dimensional ion crystals in a Penning trap*, Ph.D. thesis, Boulder, CO (2026).

[95] K. A. Gilmore, *Quantum sensing with large two-dimensional crystals of ions in a Penning trap*, Ph.D. thesis, Boulder, CO (2020).

[96] X.-P. Huang, J. J. Bollinger, T. B. Mitchell, W. M. Itano, and D. H. E. Dubin, *Physics of Plasmas* **5**, 1656 (1998).

[97] J. W. Britton, J. G. Bohnet, B. C. Sawyer, H. Uys, M. J. Biercuk, and J. J. Bollinger, *Physical Review A* **93**, 062511 (2016).

[98] A. Shankar, C. Tang, M. Affolter, K. Gilmore, D. H. E. Dubin, S. Parker, M. J. Holland, and J. J. Bollinger, *Physical Review A* **102**, 053106 (2020).

[99] A. Shankar, E. Jordan, K. A. Gilmore, A. Safavi-Naini, J. J. Bollinger, and M. J. Holland, *Physical Review A* **99**, 023409 (2019).

[100] S. B. Torrisi, J. W. Britton, J. G. Bohnet, and J. J. Bollinger, *Physical Review A* **93**, 043421 (2016).

[101] D. J. Wineland, C. Monroe, W. M. Itano, D. Leibfried, B. E. King, and D. M. Meekhof, *J. Res. Natl. Inst. Stand. Technol.* **103**, 259 (1998).

[102] B. C. Sawyer, J. W. Britton, A. C. Keith, C.-C. J. Wang, J. K. Freericks, H. Uys, M. J. Biercuk, and J. J. Bollinger, *Physical Review Letters* **108**, 213003 (2012).

[103] H. Uys, M. J. Biercuk, A. P. VanDevender, C. Osipelkaus, D. Meiser, R. Ozeri, and J. J. Bollinger, *Physical Review Letters* **105**, 200401 (2010).

[104] A. L. Carter, S. R. Muleady, A. Shankar, J. F. Lilieholm, B. B. Bullock, M. Affolter, A. M. Rey, and J. J. Bollinger, *Physical Review A* **107**, 042618 (2023).

[105] A. Polkovnikov, *Annals of Physics* **325**, 1790 (2010).

[106] J. Huber, A. M. Rey, and P. Rabl, *Physical Review A* **105**, 013716 (2022).